

# Beyond the LUMIR challenge: The pathway to foundational registration models

Junyu Chen, Shuwen Wei, Joel Honkamaa, Pekka Marttinen, Hang Zhang, Min Liu, Yichao Zhou, Zuopeng Tan, Zhuoyuan Wang, Yi Wang, Hongchao Zhou, Shunbo Hu, Yi Zhang, Qian Tao, Lukas Förner, Thomas Wendler, Bailiang Jian, Benedikt Wiestler, Tim Hable, Jin Kim, Dan Ruan, Frederic Madesta, Thilo Sentker, Wiebke Heyer, Lianrui Zuo, Yuwei Dai, Jing Wu, Jerry L. Prince, Harrison Bai, Yong Du, Yihao Liu, Alessa Hering, Reuben Dorent, Lasse Hansen, Mattias P. Heinrich, and Aaron Carass

**Abstract**—Medical image challenges have played a transformative role in advancing the field, catalyzing algorithmic innovation and establishing new performance standards across diverse clinical applications. Image registration, a foundational task in neuroimaging pipelines, has similarly benefited from the Learn2Reg initiative. Building on this foundation, we introduce the **Large-scale Unsupervised Brain MRI Image Registration (LUMIR)** challenge, a next-generation benchmark designed to assess and advance unsupervised brain MRI registration. Distinct from prior challenges that leveraged anatomical label maps for supervision, LUMIR removes this dependency by providing over 4,000 preprocessed T1-weighted brain MRIs for training without any label maps, encouraging biologically plausible deformation modeling through self-supervision. In addition to evaluating performance on 590 held-out test subjects, LUMIR introduces a rigorous suite of zero-shot generalization tasks, spanning out-of-domain imaging modalities (e.g., FLAIR, T2-weighted, T2\*-weighted), disease populations (e.g., Alzheimer’s disease), acquisition protocols (e.g., 9.4T MRI), and species (e.g., macaque brains). A total of 1,158 subjects and over 4,000 image pairs were included for evaluation. Performance was assessed using both segmentation-based metrics (Dice coefficient, 95th percentile Hausdorff distance) and landmark-based registration accuracy (target registration error). Across both in-domain and zero-shot tasks, deep learning-based methods consistently achieved state-of-the-art accuracy while producing anatomically plausible deformation fields. The top-performing deep learning-based models demonstrated diffeomorphic properties and inverse consistency, outperforming several leading optimization-based methods, and showing strong robustness to most domain shifts, the exception being a drop in performance on out-of-domain contrasts. These findings highlight the growing maturity of deep learning in neuroimaging registration and its potential to serve as a foundation model for general-purpose medical image registration.

**Index Terms**—Registration, Foundation models, Medical image challenges



## 1 INTRODUCTION

Medical image registration is a cornerstone of medical image analysis, enabling voxel correspondence between images to support a wide range of critical clinical applications. For brain magnetic resonance imaging (MRI) in particular, accurate registration plays a pivotal role in longitudinal monitoring of neurodegenerative diseases, assessing treatment effects, planning neurosurgical interventions, and conducting population-level studies of brain structure and function. By aligning serial scans or images from different subjects, registration allows precise tracking of subtle anatomical changes over time, which is essential for early

- J. Chen, Y. Dai, J. Wu, Y. Du, and H. Bai are with the Department of Radiology and Radiological Science, Johns Hopkins Medical School, Baltimore, MD, USA.
- S. Wei, J. L. Prince, and A. Carass are with the Image Analysis and Communications Laboratory in the Department of Electrical and Computer Engineering, Johns Hopkins University, Baltimore, MD, USA.
- J. Honkamaa and P. Marttinen are with the Department of Computer Science, Aalto University, Espoo, Uusimaa, Finland.
- H. Zhang is with Cornell University, New York, NY, USA.
- M. Liu is with the College of Electrical and Information Engineering, and the National Engineering Research Center of Robot Visual Perception and Control Technology, Hunan University, Changsha, Hunan, China.
- Y. Zhou and Z. Tan are with Canon Medical Systems (China) Co. Ltd., Beijing, China.
- Z. Wang and Y. Wang are with the School of Biomedical Engineering, Shenzhen University Medical School, Shenzhen, Guangdong, China.
- H. Zhou and S. Hu are with the School of Information Science and Engineering, Linyi University, Linyi, Shandong, China.
- Y. Zhang and Q. Tao are with the Department of Imaging Physics, Delft University of Technology, Delft, South Holland, Netherlands.
- L. Förner and T. Wendler are with the Department of Diagnostic and Interventional Radiology and Neuroradiology, and the Clinical Computational Medical Imaging Research group, University Hospital Augsburg, Augsburg, Bavaria, Germany. T. Wendler is also with the Institute of Digital Medicine, University Hospital Augsburg, Augsburg, Bavaria, Germany.
- B. Jian and B. Wiestler are with the Technical University of Munich, and Klinikum Rechts der Isar, Munich, Bavaria, Germany.
- T. Hable, W. Heyer, and M. P. Heinrich are with the Institute of Medical Informatics, University of Lübeck, Lübeck, Schleswig-Holstein, Germany.

- J. Kim and D. Ruan are with the Department of Radiology and the Center for Computer Vision and Imaging Biomarkers, University of California, Los Angeles, CA, USA.
- F. Madesta and T. Sentker are with the Institute for Applied Medical Informatics and the Institute of Computational Neuroscience, University Medical Center Hamburg, Hamburg, Germany.
- L. Zuo and Y. Liu are with the Department of Electrical and Computer Engineering, Vanderbilt University, Nashville, TN, USA.
- A. Hering is with the Radboud University Medical Center, Nijmegen, Gelderland, Netherlands.
- R. Dorent is with the Department of Neurosurgery at Brigham & Women’s Hospital and Harvard Medical School, Boston, MA, USA.
- L. Hansen is with EchoScout GmbH, Lübeck, Schleswig-Holstein, Germany.

Corresponding author: Junyu Chen [jchen245@jhmi.edu](mailto:jchen245@jhmi.edu).

diagnosis, disease progression modeling, and evaluation of therapeutic responses.

Over the past decade, deep learning has driven substantial progress in medical image registration, significantly improving both speed and accuracy. Among its many applications, deformable image registration for brain MRI has garnered particular attention, supported by the availability of large imaging datasets and well-established preprocessing pipelines. These advances have fueled efforts to build more precise and efficient registration models that can serve both research and clinical needs.

Although brain image registration is widely recognized as a fundamental tool in neuroimaging for applications ranging from Alzheimer’s disease research to functional mapping for surgical planning, it is often perceived as less technically challenging compared to registration tasks involving other anatomical regions. This perception stems from the fact that the brain is encased within the rigid skull, which limits large deformations and constrains anatomical variability both within and between subjects after affine pre-alignment. However, this apparent simplicity belies significant challenges. High-precision alignment of fine-scale anatomical structures, especially for small and morphologically variable structures such as the hippocampus, putamen, and amygdala. These structures often lack strong intensity-based contrast, complicating voxel-based alignment. In addition, neurodegenerative conditions introduce cortical thinning, atrophy, and other subtle deformations that demand highly sensitive and robust registration algorithms to capture clinically meaningful changes.

Medical image challenges have played a crucial role in advancing the field by providing rigorous evaluation frameworks and standardized benchmarks, fostering collaboration, driving innovation, and encouraging the development of robust and generalizable algorithms for various imaging tasks [1]–[6]. However, despite the fundamental role of image registration in many clinical and research applications, it has been relatively underrepresented in medical image challenges, particularly those focused on brain MRI. While existing challenges have extensively addressed segmentation tasks involving tumors [7], lesions [7]–[11], brain tissue [11], [12], and the parcellation of fine brain structures [13], fewer efforts have been dedicated to systematically evaluating registration algorithms for brain MRI. Notable exceptions, such as Hippocampus-MR and OASIS from previous editions of the Learn2Reg challenge [6], have offered valuable contributions but are limited in scope. For example, they focus on small regions of interest or rely on label maps that can inadvertently bias models towards over-optimizing label overlap [14] at the expense of generating smooth and physically plausible deformations [14], [15].

To address these limitations, we introduce the Large-scale Unsupervised Brain MRI Image Registration (LUMIR) challenge. This initiative offers an extensive dataset designed to support unsupervised learning of inter-subject brain MRI registration, emphasizing both anatomical accuracy and deformation smoothness without reliance on label map supervision. By offering a comprehensive and rigorously curated dataset along with gold-standard evaluation metrics, the LUMIR challenge establishes a critical platform for benchmarking and advancing the next generation of

brain image registration models, with the ultimate goal of enhancing clinical workflows and supporting high-impact neuroimaging research.

The challenge features 4,014 T1-weighted (T1-w) brain MRI images, with 3,384 training images that generate more than 5.5 million unique image pairs. This unprecedented scale promotes the development of foundational registration models while enabling fair benchmarking of traditional optimization-based and deep learning-based approaches. Furthermore, to complement the label maps used to assess accuracy, the LUMIR challenge also provides a subset of 130 test images, each manually annotated with 32 anatomical landmarks. These landmarks enable gold-standard evaluations of registration accuracy and allow analyses of correlations between landmark-based and label map-based measures. Detailed descriptions of the LUMIR challenge dataset are provided in Fig. 2. Through extensive evaluation, the results reveal that **deep learning-based methods achieve superior performance and efficiency**, with the top-performing approaches employing a single-step, optimization-free strategy (e.g., no instance-specific optimization) while producing smooth and even diffeomorphic deformations. These findings underscore the advances and maturity of deep learning methods for brain image registration.

Beyond the in-domain test set, the LUMIR challenge provides the opportunity to explore a broader and more ambitious question: **Can deep learning models trained on this large-scale dataset effectively register brain images across various modalities, acquisition protocols, and even species?** This exploration is grounded in the unique nature of image registration, which focuses on identifying spatial correspondences between image pairs. Unlike tasks that rely on the semantic interpretation of individual images, registration models prioritize inter-image relationships and transformations to align voxel grids. This characteristic suggests that these models may be inherently robust to out-of-distribution samples. To support this idea, previous studies have shown that deep learning models trained with random shapes can perform remarkably well on brain MRI registration tasks [16]. To further investigate this robustness, we evaluated challenge submissions and baseline registration models on extensive out-of-distribution brain MRI datasets. The results are striking: **deep learning methods trained solely on T1-w brain MRI images of healthy subjects performed exceptionally well and effectively generalized to out-of-domain brain images with different contrasts, resolutions, pathologies, and even across species.** Moreover, the top-performing deep learning methods significantly outperformed traditional pairwise optimization methods, which are unsupervised and theoretically should not suffer from domain shift issues. Our results directly address concerns that deep learning-based registration methods may struggle to generalize across datasets [17]. In contrast, **our findings demonstrate that with sufficient training data, learning-based registration models exhibit excellent out-of-domain generalization**, even surpassing modality-agnostic models such as SynthMorph [16]. This robustness suggests that specialized modality-agnostic training strategies may become less critical when leveraging large-scale datasets.

The LUMIR challenge underscores the transformative

potential of deep learning in creating robust and generalizable solutions for medical image registration. By addressing critical limitations in training data, evaluation methods, and application scope, this challenge establishes an unparalleled platform for benchmarking and advancing brain image registration models. This work not only summarizes the challenge outcomes but also provides empirical insights to guide the development of robust and adaptable registration models, unlocking new possibilities for clinical and research advancements.

## 2 RESULTS

In the following, we summarize the results from both the challenge test set and the zero-shot out-of-domain datasets, which exhibit substantial distributional shifts relative to the training data. Together, these evaluations provide a comprehensive benchmark for evaluating deformable image registration models in neuroimaging applications.

The evaluation phase of the challenge received submissions from 11 teams, of which only one employed a purely optimization-based method; the remaining ten submissions were deep learning-based. Among these, two incorporated instance-specific optimization, where the deformation fields predicted by the network were further refined through pairwise optimization at inference time. All submitted methods employed normalized cross-correlation (NCC) as the similarity metric for registration. In addition to participant submissions, we evaluated ten widely used baseline methods, including traditional optimization-based approaches such as SyN [18] and representative deep learning models such as VoxelMorph [19]. We include an eleventh baseline method of no deformation, `ZeroDisplacement`, to establish how the images differ prior to registration. Figure 3 presents representative qualitative results from the challenge test set and the zero-shot evaluation tasks, showcasing the outputs of the top three performing methods for each main task. A detailed description of all the evaluated methods is provided in Sec. 4.4, and a summary of the properties of each method is in Table 4.

### 2.1 Challenge Test Set

The LUMIR challenge test set comprises images drawn from the same distribution as the training data, which consists exclusively of T1-weighted brain MRIs from healthy controls. The test set includes 590 images, of which 460 are annotated with anatomical label maps and 130 with landmark points. Using these annotations, we evaluated the registration performance based on segmentation overlap and landmark alignment, quantified by Dice Similarity Coefficient (DSC) and Total Registration Error (TRE), respectively. To further assess robustness, we report the 30<sup>th</sup> percentile of these metrics (DSC30 and TRE30), highlighting performance on more challenging cases. Deformation smoothness is quantified using the non-diffeomorphic volume (NDV). Details of the dataset are provided in Sec. 4.1.1, and a full description of the evaluation metrics is presented in Sec. 4.2.

The test set results are summarized in Table 1, with a more detailed ranking presented in Fig. 1. The top ten methods demonstrated comparable registration accuracy,

with DSC scores ranging from 0.76 to 0.79, HD95 between 3.40 and 3.00, and TRE between 3.15 and 3.00. Even for more challenging cases, reflected by DSC30 and TRE30, the performance differences among the top ten methods remained similar.

Overall, deep learning-based methods outperformed traditional optimization-based approaches, with all top ten methods being DL-based. Among these, eight were developed by participants, and two were baseline models: VFA  and TransMorph , ranking 4<sup>th</sup> and 10<sup>th</sup>, respectively. The highest-ranked optimization-based method was FireANTsGreedy , which placed 12<sup>th</sup>, followed by the participant-developed optimization method VROC  in 13<sup>th</sup> place.

The top three methods in overall registration accuracy were honkamj  (1<sup>st</sup>), MadeForLife  (2<sup>nd</sup>), and LYU1  (3<sup>rd</sup>). For DSC30, the top performers were honkamj  (1<sup>st</sup>), followed by MadeForLife , LYU1 , and next-gen-nn , which were all tied for 2<sup>nd</sup>. Of particular note, next-gen-nn  ranked 5<sup>th</sup> overall, however, it performed better on the more difficult cases. For TRE30, the top three methods were MadeForLife  (1<sup>st</sup>), honkamj  (2<sup>nd</sup>), and DutchMasters  (3<sup>rd</sup>), reflecting a slight change in the classification between segmentation-based and landmark-based evaluations.

In terms of deformation regularity, VoxelMorph  is a widely used deep learning baseline that uses a diffusion regularizer to constrain the deformation fields. It produced deformation fields with approximately 1% non-diffeomorphic volumes within the brain region. All other top-performing methods generated smoother fields, with the top three methods achieving an NDV well below 1%, approaching diffeomorphic quality. Notably, all optimization-based methods excelled in generating smooth deformation fields.

### 2.2 Zero-shot Out-of-domain Evaluation Tasks

#### 2.2.1 Diverse T1-w MRI Data Sources

The first and smallest step we can take in establishing if these methods are approaching foundation model ability is to see how they behave on a T1-w dataset that is distinct from the available T1-w training data made available for the Challenge. In essence, this is the first (and easiest) obstacle that these methods have to overcome to be considered foundational. To assess this, we compare the results on the Challenge test set with T1-w inter-subject results from the NIMH dataset. These results are shown in Tables 1 and A12, specifically by looking at the comparable columns of DSC, HD95, and also DSC30. The top four methods for the Challenge test set are honkamj  (1<sup>st</sup>), MadeForLife  (2<sup>nd</sup>), next-gen-nn  (3<sup>rd</sup>), and VFA  (4<sup>th</sup>). These same four methods are also the top four methods on the T1-w NIMH inter-subject data with the order changing slightly: honkamj  (1<sup>st</sup>), VFA  (2<sup>nd</sup>), MadeForLife  (3<sup>rd</sup>), and next-gen-nn  (4<sup>th</sup>). For all four methods, their DSC values are almost identical between the two datasets, the biggest change being MadeForLife  with a difference of 0.003 between the mean DSCs for the two cohorts. For HD95, honkamj , MadeForLife , next-gen-nn , and VFA , all experienced an almost identical drop in

Submissions	Challenge Dataset				Zero-shot Dataset												Rank
	Intersubject				Intersubject			Atlas 2 Subject			Subject 2 Atlas						
	ACC	NDV	DSC30	TRE30	ACC	NDV	DSC30	ACC	NDV	DSC30	ACC	NDV	DSC30				
Bailiang	11	17	6	5	6	17	4	6	17	4	4	18	1	1			
next-gen-nn	5	9	2	5	3	9	3	13	7	13	5	9	8		2		
honkamj	1	12	1	2	2	11	1	2	11	3	1	11	4		3		
LoRA-FT	18	11	17	5	19	13	17	16	15	13	15	11	14		4		
MadeForLife	2	15	2	1	1	15	1	5	14	7	3	16	2		5		
lukast	8	20	9	5	8	20	8	8	20	4	11	20	8		6		
LYU1	3	16	2	5	5	16	4	11	16	13	9	15	10		7		
TimH	15	1	16	5	16	1	18	17	1	17	17	1	17		8		
VROC	13	18	9	5	13	19	12	21	19	21	21	19	21		9		
DutchMasters	7	13	8	3	4	11	4	1	12	1	2	14	3		10		
zhuoyuanw210	6	14	6	5	9	14	8	4	13	6	6	13	7		11		
<b>Baseline Methods</b>															12		
ANTsSyN	20	1	21	20	12	1	14	9	1	9	14	1	14		13		
DeedsBCV	19	7	20	5	21	7	20	20	9	20	20	8	20		14		
FireANTsGreedy	12	1	13	5	14	1	13	12	1	10	13	1	12		15		
FireANTsSyN	16	6	14	5	18	6	14	15	6	16	16	6	16		16		
SynthMorph	17	5	18	5	17	5	19	18	5	18	18	5	19		17		
TransMorph	10	21	9	5	10	21	10	10	21	7	10	21	5		18		
uniGradICON	14	7	15	5	15	7	14	14	7	10	12	7	12		19		
uniGradICONiso	9	9	12	4	11	10	10	3	10	1	8	10	6		20		
VFA	4	19	5	5	7	18	7	7	18	10	7	17	10		21		
VoxelMorph	21	22	19	20	20	22	20	19	22	19	19	22	18		22		
ZeroDisplacement	22	1	22	22	22	1	22	22	1	22	22	1	22				

Fig. 1. Shown for each subtask is a ranking for registration accuracy (ACC), 30<sup>th</sup> percentile of Dice Similarity Coefficient (DSC30), non-diffeomorphic volume (NDV), and 30<sup>th</sup> percentile of total registration error (TRE30), across all 21 reported methods and the baseline of no registration (`ZeroDisplacement` ). For descriptions of the 21 reported methods, see Sec. 4.5 for the eleven Challenge submissions and Sec. 4.6 for the ten Baseline methods. On the right hand side is the colormap used in the plot. For a complete description of the reported statistics and the how the ranking scheme was computed see Sec. 4.2.

performance of approximately 0.3mm. Across nearly all the methods, there is stability in the DSC and HD95 between the two cohorts of T1-w images. With respect to the DSC, the biggest changes between the two cohorts occur with `ANTsSyN`  and `VoxelMorph` , with changes of approximately 0.04 and 0.01, respectively. With three methods seeing a change of approximately 0.007 (`LoRA-FT` , `DutchMasters` , and `uniGradICON` ) , with other methods seeing a change of 0.003 or less. For HD95 the change for all methods, except `ANTsSyN` , is very uniform with an approximate change of 0.3mm; with `ANTsSyN` 

having a change of 0.5mm. However, the most interesting observation from these results is that while the DSC results saw a drop-off in performance, the HD95 saw a uniform improvement, which is a most surprising finding.

### 2.2.2 Pathological Brain: ADHD

Next, we evaluate the methods on the same T1-w contrast in which they were trained but in distinct cohorts, with attention deficit hyperactivity disorder (ADHD) in this section and subjects from the Alzheimer’s Disease Neuroimaging Initiative (ADNI) in the next. Although ADHD typically

TABLE 1

Shown for the challenge test set are the mean and standard deviation for the DSC, HD95, TRE, NDV, DSC30, and TRE30. Also shown is the ranking based on registration accuracy (ACC) which for the Testing set is a combination of the rankings of DSC, HD95, and TRE. For a complete description of the reported statistics and the how the ranking scheme was computed see Sec. 4.2.

Method	DSC	HD95	TRE	Ranking	NDV	DSC30	TRE30
	Mean( $\pm$ Std. Dev.)	Mean( $\pm$ Std. Dev.)	Mean( $\pm$ Std. Dev.)	(ACC)	Mean( $\pm$ Std. Dev.)	Mean( $\pm$ Std. Dev.)	Mean( $\pm$ Std. Dev.)
Bailiang	0.773( $\pm$ 0.028)	3.329( $\pm$ 0.434)	3.156( $\pm$ 0.931)	11	2.22e-02( $\pm$ 1.16e-02)	0.740( $\pm$ 0.023)	3.439( $\pm$ 0.975)
next-gen-nn	0.777( $\pm$ 0.027)	3.278( $\pm$ 0.430)	3.125( $\pm$ 0.938)	5	1.39e-04( $\pm$ 1.29e-04)	0.745( $\pm$ 0.021)	3.430( $\pm$ 0.955)
honkamj	0.785( $\pm$ 0.027)	3.035( $\pm$ 0.413)	3.088( $\pm$ 0.962)	1	2.52e-03( $\pm$ 6.08e-04)	0.753( $\pm$ 0.021)	3.389( $\pm$ 0.997)
LoRA-FT	0.735( $\pm$ 0.037)	3.733( $\pm$ 0.546)	3.235( $\pm$ 0.933)	18	3.27e-03( $\pm$ 5.57e-03)	0.692( $\pm$ 0.026)	3.526( $\pm$ 0.970)
MadeForLife	0.778( $\pm$ 0.027)	3.285( $\pm$ 0.436)	3.071( $\pm$ 0.942)	2	1.21e-02( $\pm$ 3.25e-03)	0.746( $\pm$ 0.021)	3.362( $\pm$ 0.980)
lukasf	0.764( $\pm$ 0.030)	3.422( $\pm$ 0.443)	3.144( $\pm$ 0.950)	8	2.76e-01( $\pm$ 7.98e-02)	0.728( $\pm$ 0.024)	3.436( $\pm$ 0.991)
LYU1	0.778( $\pm$ 0.027)	3.246( $\pm$ 0.427)	3.132( $\pm$ 0.953)	3	1.50e-02( $\pm$ 3.70e-03)	0.745( $\pm$ 0.020)	3.427( $\pm$ 0.994)
TimH	0.730( $\pm$ 0.027)	3.569( $\pm$ 0.410)	3.193( $\pm$ 0.939)	15	0.00e+00( $\pm$ 0.00e+00)	0.698( $\pm$ 0.019)	3.492( $\pm$ 0.967)
VROC	0.760( $\pm$ 0.029)	3.630( $\pm$ 0.499)	3.225( $\pm$ 0.980)	13	4.75e-02( $\pm$ 3.06e-02)	0.726( $\pm$ 0.024)	3.532( $\pm$ 1.014)
DutchMasters	0.770( $\pm$ 0.033)	3.256( $\pm$ 0.456)	3.114( $\pm$ 0.967)	7	3.02e-03( $\pm$ 1.59e-03)	0.731( $\pm$ 0.027)	3.409( $\pm$ 1.009)
zhuoyuanw210	0.773( $\pm$ 0.027)	3.233( $\pm$ 0.434)	3.143( $\pm$ 0.935)	6	4.47e-03( $\pm$ 1.37e-03)	0.740( $\pm$ 0.022)	3.434( $\pm$ 0.973)
ANTsSyN	0.703( $\pm$ 0.059)	3.688( $\pm$ 0.577)	3.484( $\pm$ 1.062)	20	0.00e+00( $\pm$ 0.00e+00)	0.633( $\pm$ 0.055)	3.845( $\pm$ 1.068)
DeedsBCV	0.696( $\pm$ 0.026)	3.945( $\pm$ 0.410)	3.104( $\pm$ 0.981)	19	1.68e-04( $\pm$ 3.72e-04)	0.665( $\pm$ 0.019)	3.424( $\pm$ 1.000)
FireANTsGreedy	0.752( $\pm$ 0.030)	3.671( $\pm$ 0.491)	3.152( $\pm$ 0.958)	12	0.00e+00( $\pm$ 0.00e+00)	0.717( $\pm$ 0.022)	3.466( $\pm$ 0.975)
FireANTsSyN	0.749( $\pm$ 0.030)	3.729( $\pm$ 0.515)	3.174( $\pm$ 0.952)	16	3.40e-05( $\pm$ 2.60e-05)	0.714( $\pm$ 0.021)	3.476( $\pm$ 0.979)
SynthMorph	0.722( $\pm$ 0.028)	3.614( $\pm$ 0.463)	3.228( $\pm$ 0.938)	17	1.12e-05( $\pm$ 1.31e-05)	0.688( $\pm$ 0.019)	3.514( $\pm$ 0.983)
TransMorph	0.762( $\pm$ 0.030)	3.462( $\pm$ 0.457)	3.142( $\pm$ 0.951)	10	3.62e-01( $\pm$ 8.70e-02)	0.726( $\pm$ 0.023)	3.439( $\pm$ 0.988)
uniGradICON	0.742( $\pm$ 0.036)	3.575( $\pm$ 0.526)	3.240( $\pm$ 0.937)	14	8.40e-05( $\pm$ 1.23e-04)	0.699( $\pm$ 0.028)	3.522( $\pm$ 0.983)
uniGradICONiso	0.760( $\pm$ 0.032)	3.401( $\pm$ 0.479)	3.135( $\pm$ 0.961)	9	1.65e-04( $\pm$ 2.21e-04)	0.721( $\pm$ 0.025)	3.421( $\pm$ 1.012)
VFA	0.777( $\pm$ 0.027)	3.150( $\pm$ 0.422)	3.138( $\pm$ 0.944)	4	7.04e-02( $\pm$ 4.67e-02)	0.744( $\pm$ 0.020)	3.428( $\pm$ 0.984)
VoxelMorph	0.714( $\pm$ 0.036)	4.072( $\pm$ 0.578)	3.528( $\pm$ 0.968)	21	1.22e+00( $\pm$ 2.69e-01)	0.671( $\pm$ 0.023)	3.851( $\pm$ 0.982)
ZeroDisplacement	0.555( $\pm$ 0.038)	4.915( $\pm$ 0.556)	4.384( $\pm$ 1.028)	22	0.00e+00( $\pm$ 0.00e+00)	0.510( $\pm$ 0.024)	4.772( $\pm$ 0.984)

does not cause distinct anatomical changes that can be clearly observed at the individual level in structural MRI scans, we included this dataset because it focuses on a specific age group, namely children aged 8 to 12, whose brain anatomy can differ substantially from that of adults. Although the training dataset does include subjects within this age range, as shown in Sec. 4.1.1, they represent a relatively small portion of the overall data. This setup allows us to assess whether the registration models can perform well on this specific subset, despite the imbalance in age representation during training.

The detailed scores for inter-subject, atlas-to-subject, and subject-to-atlas registration are shown in Tables A1, A2, and A3, respectively. For inter-subject registration, the top three performing methods are honkamj, VFA, and MadeForLife, all of which are deep learning-based. Compared to the challenge test set, we observed a slight degradation in DSC and HD95 performance, with DSC decreasing by less than 0.01 and HD95 by less than 0.05. This suggests potential influences from dataset shift, as well as the focus on a younger age group. Interestingly, ANTsSyN performed notably better on this dataset than on the challenge test set, showing an improvement of 0.031 (4%) in DSC and 0.205 (6%) in HD95. Despite this improvement, it still did not outperform deep learning-based methods and was ranked 15<sup>th</sup> overall.

For atlas-based registration tasks, the top three performing methods are honkamj, DutchMasters, and zhuoyuanw210 for atlas-to-subject registration, and Bailiang, next-gen-nn, and zhuoyuanw210 for the subject-to-atlas registration task. Interestingly, we observe that all methods perform better, or at least equally well (with equal scores likely due to the inverse consistency constraint enforced by some methods), on the subject-to-atlas task than the atlas-to-subject task. However, the specific reason for this performance asymmetry remains

unclear.

### 2.2.3 Pathological Brain: ADNI

Subjects with mild cognitive impairment and Alzheimer’s disease often present with significant brain atrophy, ventricular enlargement, and other structural changes compared to healthy controls. These anatomical changes introduce a significant domain shift relative to structurally normal training data, posing substantial challenges for deep learning-based registration models. Evaluating zero-shot performance on these pathological cases provides valuable insight into how effectively deep learning-based registration models generalize beyond their training domain. Our evaluation includes both 1.5T and 3T MRI scans, allowing for an assessment of model robustness across different field strengths. The detailed scores for inter-subject, atlas-to-subject, and subject-to-atlas registration are reported in Tables A4, A5, A6, A7, A8, and A9.

For all three registration tasks, the top-performing methods were based on deep learning. For inter-subject registration, the top-performing methods for both 1.5T and 3T scans were honkamj, MadeForLife, and next-gen-nn. For atlas-to-subject registration, the top-performing methods across both field strengths were DutchMasters, honkamj, and VFA. For subject-to-atlas registration, the top three methods for 1.5T were DutchMasters, MadeForLife, and honkamj, while for 3T they were DutchMasters, honkamj, and Bailiang. Despite the anatomical variability associated with neurodegeneration, the top-performing deep learning-based methods consistently outperformed traditional optimization-based approaches across all registration tasks. The similar performance observed between the 1.5T and 3T results further suggest that incorporating training data from both field strengths enhances model generalizability across different acquisition protocols.

### 2.2.4 Out-of-Domain MRI Contrasts

Out-of-domain contrast tests include intra-contrast registration tasks within one of T2-weighted (T2-w), T2\*-weighted (T2\*-w), and FLAIR, all of which come from the NIMH dataset; this is an out-of-domain task as the methods have been trained on only T1-weighted (T1-w) intra-contrast registration. We want to see if the methods generalize well to unseen contrasts and maintain the same level of accuracy as the in-domain contrast. Using DSC and HD95 as our proxies for accuracy, we see an almost uniform drop in the performance characteristics of the various methods between the intra-contrast registration on the T1-w data and the intra-contrast registration with the other contrasts. We see this based on comparing the intra-contrast results on the T1-w data (Table A12) with any of the intra-contrast results for the other three contrasts (Table A13 for T2\*-w, Table A14 for T2-w, or Table A15 for FLAIR). The only exception is DeedsBCV , which had slightly better mean DSC and HD95 for intra-contrast registration with the T2-w images than it had for intra-contrast registration with the T1-w images.

A key observation from examination of Tables A12 through A15, is that while all methods see a degradation in performance (except DeedsBCV  in one sub-task), the impact varies considerably; this is readily discernible from the change in the ordering of the methods in these tables. Consider the top three performing methods with respect to the T1-w inter-subject task, they are honkamj , VoxelMorph , and MadeForLife . However, the same methods have dramatically different rankings (and as noted above poorer performance) on the inter-subject task for the T2\*-w images. Specifically, honkamj  drops to 7<sup>th</sup>, VoxelMorph  falls dramatically to 20<sup>th</sup>, while MadeForLife  manages to move up to rank 2<sup>nd</sup> despite its own drop in performance; this is due to the much greater performance drop of the other methods. Similar changes in the rankings are obvious when considering any methods across the NIMH collection of sub-tasks. It might be argued that the issue is not with the methods, but rather with the choice of statistics; however, this is not borne out by a review of the statistics used or by replacing those statistics with more robust counterparts. Firstly, the issue of the inconsistency in the rankings exists in HD95 which itself is already a robust statistic on the Hausdorff distance. Secondly, if we look at the DSC30 which is a robust statistic on the Dice Similarity Coefficient, we again see drops in performance and large changes in the rankings between the T1-weighted contrast and any of the other contrasts. For example, the DSC30 on the intra-contrast sub-task on the NIMH data has the top three methods being honkamj , MadeForLife , and next-gen-nn . While for the T2\*-w registration sub-task, with respect to DSC30, honkamj  drops to 7<sup>th</sup>, MadeForLife  moves up to 1<sup>st</sup>, and next-gen-nn  drops to 9<sup>th</sup>. In fact, for each of the inter-subject sub-tasks on the NIMH data, the ranking of the methods for both DSC and DSC30 is almost identical; which is not the case when looking at rankings between the different sub-tasks. These drops in performance and chaotic changes in the ranking when applying the methods to the NIMH zero-shot tasks highlight that there is still work to be done

to establish foundational models for registration that are robust to imaging contrast.

### 2.2.5 Ultra-High-Field MRI

Recent advances in high-field and ultra-high-field MRI technologies are enabling neuroimaging at substantially improved spatial resolution and tissue contrast compared to conventional 1.5T or 3T MRI scanners. These improvements allow for better separation of fine anatomical structures, but they also introduce domain shifts in image appearance that can challenge registration algorithms. In neuroimaging studies using high- or ultra-high-field MRIs, accurate registration is critical, and it is desirable for top-performing deep learning-based registration models to generalize to these new imaging modalities without requiring retraining.

To assess the robustness of the submitted models, we evaluated their zero-shot performance on the UltraCortex 9.4T dataset across three registration tasks: inter-subject, atlas-to-subject, and subject-to-atlas registration. The results of each task are summarized in Tables A16, A17, and A18, respectively.

Inter-subject registration is inherently the most challenging due to anatomical variability. As expected, overall Dice scores were lower across the three subtasks. In the inter-subject registration task, honkamj  achieved the top performance, leading both in terms of DSC and HD95, earning 1<sup>st</sup> place overall. Close competitors included MadeForLife  and VFA , which also demonstrated high DSC scores and reasonably low HD95 values, indicating strong spatial alignment. In particular, VFA  achieved these results with a relatively high NDV, suggesting some trade-off between anatomical plausibility and spatial accuracy.

In the atlas-to-subject registration task, honkamj  again led with the highest accuracy ranking, while maintaining anatomical plausibility with a low NDV. MadeForLife  and VFA  closely followed in performance, showing similarly high DSC scores and low HD95 values, affirming their robustness across tasks. Notably, VFA ’s relatively high NDV shows again its tendency towards less regularized deformation.

The subject-to-atlas registration task shows slightly better performance across methods compared to atlas-to-subject registration, indicating that the direction of registration affects accuracy. MadeForLife  claimed the highest accuracy ranking, closely followed by next-gen-nn  and VFA . These top-performing methods consistently achieved high overlap and low boundary errors, while generally keeping NDV within acceptable ranges. Notably, next-gen-nn  had one of the lowest NDVs, which emphasizes its effectiveness in preserving diffeomorphic properties while delivering high accuracy.

Overall, consistent top performers across all tasks include honkamj , MadeForLife , and VFA , which show robust registration accuracy and good diffeomorphic behavior. Registration accuracy declines from subject-to-atlas to atlas-to-subject, emphasizing the importance of evaluating across multiple directions. Deep learning methods outperform traditional methods in alignment metrics, but often at the cost of increased non-diffeomorphic deformations, unless specifically regularized.

### 2.2.6 Non-Human Species

The macaque brain inter-subject registration task involves anatomical structures that differ significantly from those in the human brain dataset. Evaluating on this dataset introduces a domain shift in structural anatomy and imaging content, beyond the intensity differences assessed in the out-of-domain contrast experiments. However, due to the differences in anatomical structures, it is not feasible to evaluate the alignment of the same types of anatomical labels as those used in the human brain datasets. Additionally, the annotations in the macaque dataset are relatively coarse, making direct performance comparisons with human brain registration results inappropriate.

Given these limitations, we discuss the results of this task separately and focus on comparing the methods directly. As shown in Table A19, without registration (i.e., ZeroDisplacement ) , the DSC is already 0.665. Most methods perform reasonably close to each other, with DSC values ranging from 0.75 to 0.78 and HD95 from 4.6 to 4.3. An exception is VFA , which, despite consistently ranking in the top ten on human brain tasks, was the only method to fall below 0.7 in DSC and above 5 in HD95, ranking lowest among all methods on this task.

The three best performing methods on the macaque dataset are MadeForLife , FireANTsGreedy , and honkamj . Notably, this is the only task in which the optimization-based method FireANTsGreedy  ranked among the top three, outperforming several deep learning-based methods that had surpassed it in the other tasks.

## 3 DISCUSSION

### Deep Learning Models Excel in Zero-Shot Registration.

Deep learning models are often considered sensitive to domain shifts; that is, when trained on data from one distribution, their performance typically declines when evaluated on data from another [20]. Addressing distributional bias remains an active research area, prompting the development of specialized techniques for domain generalization [21] and domain adaptation [22], both of which aim to improve the ability of deep learning models to generalize across different data distributions.

In the LUMIR challenge, models were trained exclusively on inter-subject registration tasks using T1-weighted brain MRIs of healthy controls. However, our zero-shot evaluations introduced significant distributional shifts by including modalities such as T2-, T2\*-, and FLAIR-weighted MRIs, as well as atlas-to-subject registration, pathological cases, and even images from non-human species. Surprisingly, the LUMIR challenge results defy conventional expectations, demonstrating substantial robustness of deep learning registration models to domain shifts. These methods (e.g., honkamj , MadeForLife , and next-gen-nn ) demonstrated remarkable robustness, consistently ranking at the top and significantly outperforming traditional optimization-based techniques in registration accuracy measured by DSC and HD95. Even in cases with substantial differences in image contrast and resolution, such as T2\* and FLAIR images, performance degradation is minimal. As shown in Fig. 1, deep learning-based approaches occupy all top-five rankings in zero-shot tasks, whereas estab-

lished optimization-based methods including ANTsSyN , DeedsBCV , and recently proposed FireANTs /, theoretically less susceptible to domain shifts due to their pairwise, iterative-optimization nature, consistently ranked lower.

We attribute the robustness demonstrated in the LUMIR challenge primarily to the substantial diversity of the training data, which was acquired from over 60 imaging centers. This broad sampling contrasts with prior findings, such as those reported in the SynthMorph study [16], where models trained on data from a single center exhibited significant performance degradation when evaluated on data from other centers. This observation motivated the modality-agnostic training strategy used in SynthMorph . However, despite its modality-agnostic approach, SynthMorph  performed poorly in the LUMIR challenge, even compared to traditional optimization-based methods on zero-shot tasks (Fig. 1). These results emphasize that, beyond modality-agnostic training strategies, the choice of model architecture remains a critical factor influencing robust registration performance.

Interestingly, the strong robustness of deep learning models was observed even when performing registrations involving substantial anatomical differences, including pathological brains (i.e., neurodegenerative diseases) and non-human species (i.e., macaque brains). We hypothesize that the observed robustness may inherently stem from the nature of the registration task itself. In particular, registration models primarily optimize for similarity metrics computed between pairs of input images, emphasizing relative differences rather than semantic content specific to individual images. In this regard, the registration task closely resembles contrastive learning paradigms.

Finally, despite excellent performance on zero-shot tasks, all tasks evaluated in the challenge remained within a single MRI contrast type. We anticipate that performance would degrade substantially on inter-contrast registration tasks (e.g., T1-weighted to T2-weighted MRI). We hypothesize that this is largely due to the training similarity metrics (such as normalized cross-correlation), which do not encourage learning of contrast-invariant features essential for robust inter-contrast registration.

**Optimization-based Methods Fall Short.** Optimization-based refers to those methods that rely on pairwise optimization without any prior training stage, and they have historically seen widespread use in neuroimaging studies. Common pipelines for statistical parametric mapping [23], voxel-based morphometry [24], brain segmentation [25], and computational anatomy [26] heavily depend on optimization-based methods. In the LUMIR challenge, the optimization-based methods evaluated included VROC , ANTsSyN , DeedsBCV , and FireANTs /. Despite their historical significance and conceptual appeal, these methods consistently underperformed compared to learning-based approaches when applied to practical neuroimaging tasks such as atlas-based registration.

On the challenge test set, ANTsSyN , a widely used optimization-based method, ranked 20<sup>th</sup> out of 21 methods, outperforming only VoxelMorph . This is consistent with the original VoxelMorph publication, which reported comparable or slightly inferior performance rela-

tive to ANTsSyN [10]. DeedsBCV [11] followed closely, ranking 19<sup>th</sup>. FireANTs [12]/[13], a recent method introduced as a strong optimization-based alternative to deep learning models, achieved only moderate rankings: 12<sup>th</sup> for its Greedy variant (FireANTsGreedy [12]) and 16<sup>th</sup> for its SyN variant (FireANTsSyN [13]). Another optimization-based method, VROC [14], specifically tuned for the LUMIR test set by challenge participants, ranked 13<sup>th</sup> overall.

On the zero-shot datasets, optimization-based methods demonstrated certain advantages. Because these methods optimize deformation fields independently for each image pair, they are inherently less sensitive to domain shifts. As such, ANTsSyN [10] and FireANTs [12]/[13] achieved higher accuracy and modest improvements in their overall rankings (see Fig. 1). Nevertheless, they consistently remained outside the top ten, with the best-performing method on each zero-shot task being deep learning-based.

Overall, these findings indicate that although optimization-based methods exhibit robustness to domain shifts, they consistently lag behind deep learning models in both accuracy and reliability. Since the introduction of VoxelMorph in 2019 [19]—when deep learning-based registration was only comparable to ANTsSyN—the field has advanced markedly. Optimization-based approaches still hold value, particularly for their well-defined properties such as symmetric deformations and explicit modeling of time-varying velocity fields. However, the deep learning methods that perform the best in the LUMIR challenge now substantially outperform these traditional techniques on a wide range of tasks. Furthermore, while domain shift remains a recognized challenge in deep learning, where dataset changes have been shown to degrade registration accuracy [17], our results suggest that models trained on sufficiently large and diverse datasets can achieve both high accuracy and strong generalization. These findings underscore the growing maturity of deep learning registration models and their readiness for deployment as practical and effective tools for quantitative neuroimaging analysis.

**Identifying Effective Model Designs.** In this section, we explore common architectural patterns among the top-performing models, based on observed trends, as direct ablation studies are not feasible. Notably, the top five models on the challenge test set—honkamj [15], MadeForLife [16], LYU1 [17], VFA [18], and next-gen-nn [19]—all adopted a dual-stream encoder design. In this setup, separate encoders are used to extract features from the moving and fixed images independently, rather than jointly feeding both images into a shared encoder. This design encourages each encoder to focus on extracting features specific to its input, without early fusion of information across the image pair. The responsibility of identifying differences between the two images is thus shifted to the decoder, which estimates the deformation field based on the contrast between the separately encoded feature maps. The results suggest a strong correlation between this architectural design and effective registration performance.

Another common feature among these models is a coarse-to-fine strategy for deformation estimation, where the deformation fields are estimated at multiple resolutions and then composed to form the final output. This hierar-

chical approach is likely beneficial for capturing both global and local deformations effectively. zhuoyuanw210 [20] which also adopts both the dual-stream and coarse-to-fine design elements, achieved a strong performance as well, ranking 6<sup>th</sup> on the challenge test set.

On the zero-shot tasks, we further observed that DutchMasters [21] and Bailiang [22]—ranked 7<sup>th</sup> and 11<sup>th</sup>, respectively, on the challenge test set—showed notable improvements, with DutchMasters [21] ranking in the top three for the atlas-based registration tasks. We speculate that this improvement may be linked to a shared design strategy: progressive registration. In this approach, the model iteratively estimates full-resolution deformation fields, gradually refining the alignment by progressively warping the moving image toward the fixed image over multiple steps.

Interestingly, all other models that adopted progressive registration maintained similar rankings across the challenge and zero-shot tasks. In contrast, models that did not employ this design, such as LYU1 [17] and next-gen-nn [19], showed significant performance drops, falling out of the top ten on several tasks. This observation underscores the potential importance of progressive registration and opens a promising avenue for future work, particularly through a controlled ablation study.

**Does Instance-Specific Optimization Improve Performance?** Since both moving and fixed images are available during training and at test time, learning-based methods can further refine the deformation field by iteratively optimizing the registration loss function for each specific image pair at test time. This process, known as instance-specific optimization (ISO), treats the DNN as an implicit optimizer corresponding to an unrolled iterative optimization procedure [27]. Conceptually, the DNN approximates the iterative optimization of a registration objective function (i.e., image similarity measure and deformation regularization) truncated after a fixed number of iterations. ISO then continues to explicitly optimize this objective function explicitly for the given image pair to achieve improved registration accuracy. Several previous studies have shown that ISO can significantly improve the performance of learning-based registration models [19], [28]. Traditional registration methods, which iteratively optimize an objective function per image pair, can also be considered as a form of ISO.

Results from the LUMIR challenge indicate that the top-performing methods on both the “in-domain” challenge test set and the “out-of-domain” zero-shot test set did not employ ISO, yet substantially outperformed methods utilizing ISO. Among ISO-based approaches, the best-performing method was DutchMasters [21], achieving the rank of 7<sup>th</sup> on the challenge test set. For the zero-shot tasks, DutchMasters [21] attained mean ranks of 4<sup>th</sup>, 1<sup>st</sup>, and 5<sup>th</sup> for DSC, and 4<sup>th</sup>, 2<sup>nd</sup>, and 1<sup>st</sup> for HD95 across intersubject, atlas-to-subject, and subject-to-atlas tasks, respectively. Clearly, this method exhibited enhanced robustness in the zero-shot datasets, even reaching top performance in several instances. Such improvements could be attributed to ISO bridging performance gaps caused by data distribution shifts. Nonetheless, the overall best-performing method, honkamj [15], did not use ISO.

Although direct ablation studies were not feasible for the participant-submitted methods, the analysis of the baseline

method `uniGradICON` clearly showed the beneficial impact of ISO. The ISO component improved the rankings by five places (14<sup>th</sup>  $\rightarrow$  9<sup>th</sup>) for the challenge test set, alongside noticeable gains for the zero-shot set. However, a clear disadvantage of ISO is its substantial computational burden, resulting in significantly increased runtimes. For instance, the runtime for `honkamj` was 56.87s per image, compared to 1604.29s for `DutchMasters` using a CPU, although employing GPUs is expected to significantly alleviate this runtime overhead. Overall, these findings emphasize that while ISO can enhance robustness and model performance, optimal DNN design that integrates inductive bias relevant to image registration continues to play a critical role in achieving the best performance.

**Deformation Regularity.** Deformation regularization plays a crucial role in ensuring that estimated transformations are anatomically plausible. Without appropriate constraints, deformable registration algorithms may produce biologically unrealistic mappings, such as foldings, even when achieving high image similarity. While the assumption of smooth, invertible deformations may not hold in cases of severe brain pathology, it is well-justified in the context of this challenge, which focuses primarily on healthy subjects and individuals with neurodegenerative conditions such as Alzheimer’s disease and mild cognitive impairment. In these populations, overall brain topology is largely preserved, and the transformations used to register them are expected to be diffeomorphic. To quantify deformation regularity, we compute the Non-Diffeomorphic Volume (NDV) [29] for each estimated transformation; NDV represents the proportion of folded volume relative to the total brain volume. It is important to note that a zero NDV confirms the absence of folding but does not imply that the registration is accurate. Conversely, a non-zero NDV provides direct evidence of anatomically implausible behavior in the affected region(s).

Across the test and zero-shot datasets,  $\text{NDV} \geq 1\%$  was exceedingly rare. The only method exhibiting such levels of folding was `VoxelMorph`. In contrast, even methods that do not incorporate explicit diffeomorphic constraints or specialized regularization strategies were still able to achieve  $\text{NDV} \leq 1\%$ . As registration methods continue to improve in accuracy, we expect to observe a corresponding reduction in non-diffeomorphic volume.

Among all submissions, deep learning-based `TimH` and optimization-based `ANTsSyN` consistently produced perfectly diffeomorphic transformations (i.e.,  $\text{NDV} = 0$ ) across all evaluated cases. Additionally, methods that incorporate inverse-consistency constraints (as discussed in the following paragraph) generally outperformed those that do not in terms of deformation regularity. While deformation regularization has traditionally been viewed as being in tension with registration accuracy, we found that the top-performing methods on each dataset were not those with the highest NDV. This indicates that, with thoughtful architectural or algorithmic design, it is possible to simultaneously improve registration accuracy and reduce non-diffeomorphic regions.

**Inverse Consistency.** Inverse consistency (IC) has long been considered a key constituent part of the registration of medical images; IC simply means that whatever deformation you get in going from image  $A$  to image  $B$ , should be the inverse

of the deformation that you get in going from  $B$  to  $A$  (that is, the combination of these two deformations should be the identity transform). The rationale for the importance of this is the preservation of anatomical landmarks when moving between the images of two patients; there are several other benefits and implications of IC that are discussed in greater detail in [15], [30].

While IC is conceptually related to deformation regularity, it is distinct from diffeomorphism. A deformation can be inverse consistent without being smooth, whereas diffeomorphisms impose additional constraints such as smoothness and invertibility. Therefore, when evaluating IC, we do not rely on measures such as non-diffeomorphic volume (NDV) [29], which assess diffeomorphic properties rather than inverse consistency. Despite its desirable properties, IC is not inherently guaranteed in most modern deep learning-based registration models. Without explicit architectural designs or dedicated loss terms enforcing IC, neural networks typically generate different deformation fields when the order of the input images is swapped. Formally, if we define the deformation field mapping image  $A$  to image  $B$  as  $\phi_{A \rightarrow B} = \text{DNN}(A, B)$ , inverse consistency requires that  $\phi_{A \rightarrow B} = \phi_{B \rightarrow A}^{-1}$ . However, this condition generally does not hold for DNN models, even when the generated deformation fields are diffeomorphic.

In the LUMIR challenge, three evaluated methods explicitly guarantee IC by design: `honkamj` and `TimH`, and `ANTsSyN` (see Table 4). Specifically, `honkamj` and `TimH` achieve IC through an auxiliary network structure that computes deformation fields by exponentiating the difference of intermediate fields generated with reversed input orders. In contrast, the optimization-based method `ANTsSyN` ensures IC by simultaneously optimizing forward and inverse deformation maps in a symmetric manner.

Furthermore, four methods encourage IC through regularization: `LoRA-FT`, `DutchMasters`, `uniGradICON`, and `uniGradICONiso`. These methods employ the GradICON regularizer [31], which penalizes deviations of the Jacobian of the composed forward and inverse maps from the identity. However, as noted in [31], GradICON represents a relaxed version of IC regularization, penalizing derivatives of deformation rather than strictly enforcing inverse consistency. Thus, even when the Jacobian of the composed deformation fields approaches identity (i.e.,  $\nabla(\phi_{A \rightarrow B} \circ \phi_{B \rightarrow A}) = Id$ ), residual spatial drifts in the composed deformation remain permissible. Therefore, while GradICON-based methods tend to produce smooth deformations, they do not explicitly enforce inverse consistency.

Importantly, even if a method is theoretically inverse consistent, overlap-based segmentation metrics applied to the resulting warped label maps may still differ between forward and inverse directions. In theory, segmentation metrics such as DSC and HD95 are symmetric—that is,  $\text{DSC}(L_A, L_B) = \text{DSC}(L_B, L_A)$  and  $\text{HD95}(L_A, L_B) = \text{HD95}(L_B, L_A)$  for any two label maps  $L_A$  and  $L_B$ . However, in practice, evaluating registration involves interpolating label maps on a discrete voxel grid, and resampling introduces small but non-negligible differences in the warped segmentations. Consequently, the label maps being compared are not exact inverses of one another, breaking

TABLE 2

Mean absolute error (MAE) quantifying the deviation of the composed forward and inverse deformation fields from the identity, computed as  $|\phi_{A \rightarrow B} \circ \phi_{B \rightarrow A} - Id|$ . The forward and inverse fields are obtained from the “Subject to Atlas” and “Atlas to Subject” tasks, respectively.

Method	MAE	
	Mean( $\pm$ Std. Dev.)	
Bailiang	1.059	( $\pm$ 0.017)
next-gen-nn	0.646	( $\pm$ 0.033)
honkamj	0.031	( $\pm$ 0.007)
LoRA-FT	0.790	( $\pm$ 0.016)
MadeForLife	0.502	( $\pm$ 0.014)
lukasf	0.463	( $\pm$ 0.036)
LYU1	0.467	( $\pm$ 0.019)
TimH	0.040	( $\pm$ 0.007)
VROC	0.260	( $\pm$ 0.027)
DutchMasters	0.452	( $\pm$ 0.139)
zhuoyuanw210	0.488	( $\pm$ 0.042)
ANTsSyN	0.040	( $\pm$ 0.047)
DeedsBCV	0.627	( $\pm$ 0.048)
FireANTsGreedy	0.442	( $\pm$ 0.027)
FireANTsSyN	0.392	( $\pm$ 0.031)
SynthMorph	0.017	( $\pm$ 0.002)
TransMorph	0.562	( $\pm$ 0.038)
uniGradICON	0.546	( $\pm$ 0.030)
uniGradICONiso	0.681	( $\pm$ 0.174)
VFA	0.414	( $\pm$ 0.017)
VoxelMorph	0.323	( $\pm$ 0.016)
ZeroDisplacement	-	-

the symmetry in computed overlap metrics. Moreover, DSC and HD95 are sensitive to structure size and boundary sampling. For example, DSC normalizes by the union of the two segmentations; when aligning a small structure to a large one, interpolation errors can lead to disproportionately low Dice scores due to the smaller denominator. HD95, as a percentile-based boundary metric, is also more sensitive to boundary irregularities in small or sparsely sampled structures. These factors can yield asymmetric overlap metrics, even when the underlying deformation fields are nearly or exactly inverse consistent.

To address these aforementioned flaws and to provide a more direct assessment of IC, we computed the mean absolute error (MAE) between the composed deformation field and the identity map. Specifically, we evaluated the performance of each method in paired subtasks, “Atlas to Subject” and “Subject to Atlas”, across the zero-shot datasets. These tasks differ only in the order of input images; thus, an inverse-consistent method should produce deformation fields whose composition approximates the identity transformation. A lower MAE indicates stronger IC, with a value of zero corresponding to perfect consistency. Table 2 summarizes these results, with scores averaged across five datasets: ADHD, ADNI1.5T, ADNI3T, NIMH, and UltraCor-tex.

None of the evaluated methods achieved perfect IC. Even for those that guarantee IC by design—such as honkamj, TimH, and ANTsSyN—minor deviations are observed, likely due to interpolation errors during the resampling step. Nevertheless, these methods exhibited

the lowest MAE values, with honkamj, TimH, and ANTsSyN achieving mean MAEs of 0.031, 0.040, and 0.040, respectively.

In contrast, methods incorporating the GradICON regularizer—LoRA-FT, DutchMasters, uniGradICON, and uniGradICONiso—did not demonstrate strong inverse consistency, yielding mean MAEs of 0.790, 0.452, 0.546, and 0.681, respectively. Although these methods produced smooth deformation fields with low NDV values (see Table 1 and Appendix), indicating near-diffeomorphic behavior, their high MAEs confirm that GradICON does not explicitly enforce IC but rather encourages deformation regularity. Notably, their IC performance was no better, and in some cases worse, than methods that neither promote inverse consistency nor enforce diffeomorphism, such as VFA (0.414), TransMorph (0.562), and DeedsBCV (0.627).

Interestingly, the best-performing method in terms of IC was SynthMorph, with an MAE of just 0.017. To the best of our knowledge, SynthMorph neither guarantees IC by design nor includes an IC-specific regularization term. This unexpected result suggests that SynthMorph’s training strategy, particularly its use of large-scale synthetic data, may implicitly promote inverse consistency, and warrants further investigation in future studies.

**Dice versus TRE: Correlation?** Torsten Rohlfing’s 2012 paper [32] makes a compelling argument for not relying on tissue label overlap to evaluate registration accuracy. Given the broad range of registration methods available to us as organizers and the presence of both labels and landmark data in our Test Set, we have the opportunity to return to Rohlfing’s premise and see if we can offer any further insight. We choose to see if there is any correlation between the Dice Similarity Coefficient (DSC) and the Total Registration Error (TRE) on the challenge test set. We computed the Pearson correlation coefficient between the mean DSC and the mean TRE across our challenge test set, as the slope of the linear fit. The correlation and slope are reported in Table 3.

The slopes, in Table 3, are all negative, which is expected—as DSC improves, it goes up and TRE goes down, and vice versa for worsening results. However, the correlations are poor, indicating that the relationship between DSC and TRE is not particularly strong. This is not particularly surprising; first the landmarks are sparse, and the labeled structures run the gambit of small to large. Second, the landmarks are not in any reasonable correspondence with the available labels. As such, this simple analysis has informed us about how to better evaluate the relationship between DSC and TRE, if any such relationship exists. Moving forward with future challenges, we anticipate using several dedicated landmarks that are readily focused on specific structures, with the landmarks capturing the important boundary positions of the structures under investigation.

TABLE 3

The Pearson correlation coefficient (Correlation) and slope of a linear fit between the mean Dice Similarity Coefficient and the mean Total Registration Error on the Challenge Test dataset.

Method	Correlation	Slope
Bailiang	-0.080	-2.252
next-gen-nn	-0.089	-2.568
honkamj	-0.072	-2.180
LoRA-FT	-0.132	-3.113
MadeForLife	-0.078	-2.274
lukasf	-0.085	-2.312
LYU1	-0.073	-2.236
TimH	-0.125	-4.085
VROC	-0.151	-4.287
DutchMasters	-0.054	-1.361
zhuoyuanw210	-0.094	-2.856
ANTsSyN	-0.347	-6.815
DeedsBCV	-0.177	-5.994
FireANTsGreedy	-0.135	-4.016
FireANTsSyN	-0.101	-2.876
SynthMorph	-0.167	-5.428
TransMorph	-0.081	-2.291
uniGradICON	-0.126	-3.061
uniGradICONiso	-0.107	-2.847
VFA	-0.089	-2.721
VoxelMorph	-0.208	-5.246
ZeroDisplacement	-0.377	-9.926

## 4 METHODS

### 4.1 Datasets

#### 4.1.1 Challenge Dataset

The LUMIR challenge training, validation, and test data is built from three primary public sources, these include ten different public datasets [33]–[43] that are part of the OpenBHB dataset [44] and the OASIS dataset [45], in combination with public landmarks [46] and our own privately held landmarks. The OpenBHB dataset contains T1-weighted brain MRIs that have been skull-stripped and affinely aligned to the isotropic 1mm MNI template using FreeSurfer [25]. Subsequently, we applied kernel-based intensity normalization [47] to normalize the mean white matter value to 110 and used the automated segmentation tool SLANT [48] to segment the brains into 133 cortical and subcortical structures. The AFIDs-OASIS dataset [49], comprising 30 T1-weighted MRIs with 31 manually labeled anatomical landmarks per image, underwent identical pre-processing steps. The final LUMIR dataset contains 4,014 images, with 3,984 from OpenBHB and 30 from AFIDs-OASIS. From these, we randomly allocated 3,384 OpenBHB images for training; 40 images (30 from OpenBHB, 10 from AFIDs-OASIS) for validation via the grand-challenge.org public leaderboard; and 590 images (570 from OpenBHB, 20 from AFIDs-OASIS) for testing. Additionally, following AFIDs protocols [49], a neurologist (Y. Dai) and two radiologists (J. Wu, H. Bai) manually annotated landmarks on 110 OpenBHB images in the test set for landmark-based evaluation. Specifically, the final breakdown includes:

- **Training:** 3,384 unlabeled brain MRI images.

- **Validation:** 50 brain MRI images, comprising 40 with segmentation label maps and 10 with landmarks.
- **Testing:** Privately held 590 brain MRI images, including 460 images with segmentation labels and 130 images with landmark annotations.

In line with our focus on unsupervised image registration, only imaging data were provided for training (i.e., no label maps or deformation fields), allowing participants to freely create inter-subject pairs or deformation fields as they see fit. This setup yields 5,724,036 unique pairs of moving and fixed images ( $3,384 \times 3,383 / 2$ ) for training purposes. Anatomical label maps and landmarks for the training and validation sets were kept private. However, a small subset (label maps from five images) was made available to participants for preliminary sanity checks before submitting their results to the Grand Challenge platform.

#### 4.1.2 Zero-shot Dataset

- **ADHD [50], [51]:** This dataset includes MRI scans from 47 children diagnosed with attention deficit hyperactivity disorder (ADHD) in two previous studies. The cohort consists of 35 males (ages 8.59–11.85) and 12 females (ages 9.8–12.3). MRI scans were acquired using 3T and 1.5T systems with the MP-RAGE sequence.
- **ADNI1 1.5T&3T:** Subsets of the ADNI1 dataset were used, specifically the “Complete 1Yr 1.5T” and “Complete 1Yr 3T” cohorts, comprising 639 and 89 subjects, respectively, all diagnosed with Alzheimer’s disease. Scans were acquired using 1.5T and 3T MRI systems. The age range for the 1.5T cohort is 55–91 years, and for the 3T cohort, 55–89 years. ADNI1 data was obtained from the Alzheimer’s Disease Neuroimaging Initiative (ADNI) database (adni.loni.usc.edu). ADNI was launched in 2003 as a public-private partnership, led by Principal Investigator Michael W. Weiner, MD.
- **NIMH [52]:** This dataset includes MRI scans of healthy subjects aged 18–72 years. The scans were categorized by imaging modality, comprising 249 subjects with T1-weighted scans, 247 with T2-weighted scans, 241 with T2\*-weighted scans, and 240 with FLAIR scans. Notably, T2\*-weighted and FLAIR scans typically exhibit larger voxel sizes along the slice-select (z-axis) direction, leading to significantly lower resolution along this axis.
- **UltraCortex [53]:** This data set consists of 9.4T ultra-high-field T1 weighted MRI scans from 78 healthy adults (28 females, 50 males) aged 20–53 years. MRI acquisition was performed using a 9.4T whole-body scanner with the MP-RAGE and MP2RAGE sequences.
- **Atlas:** The ICBM 2009c Nonlinear Symmetric T1-weighted template with  $1 \times 1 \times 1$  mm isotropic resolution was used for atlas based registration. This template is part of the ICBM 152 Nonlinear atlases (2009 version) [54].
- **Macaque [55]:** This dataset includes T1-weighted MRI scans from 57 macaques, collected from five different sources: **1) Aix-Marseille Université:** Contains

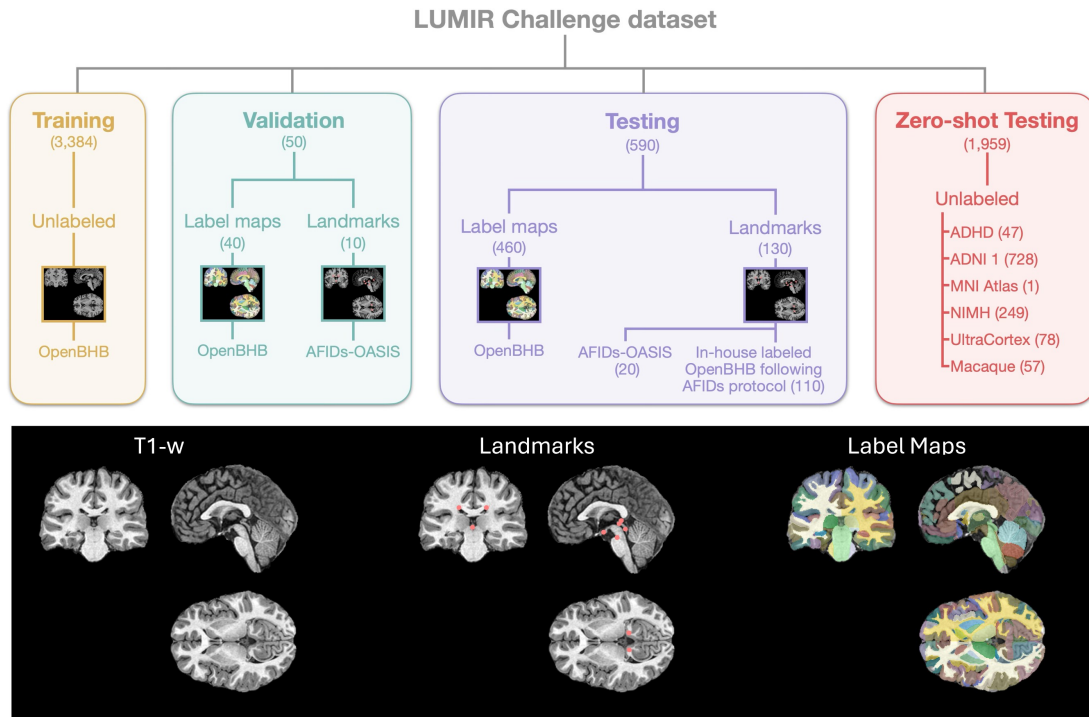


Fig. 2. The top panel provides a breakdown of the training, validation, and testing data used in the LUMIR Challenge; with each source listed and the quantity of data in parentheses. The bottom panel shows from left to right, a tri-planar view of a typical T1-weighted MRI after our preprocessing, the manually identified landmarks overlaid on the same T1-weighted MRI, and finally the corresponding SLANT labels of the T1-weighted MRI. See Sec. 4.1 for complete details.

4 scans from 3 male and 1 female *Macaca mulatta*, aged 7–8 years, acquired using a 3T MRI system with the MPRAGE sequence. **2) Mount Sinai School of Medicine (Philips):** Includes 9 scans from 8 males and 1 female *Macaca mulatta* and *Macaca fascicularis*, aged 3.4–8 years, acquired on a 3T MRI scanner with the MPRAGE sequence. **3) McGill University:** Comprises 3 scans from 3 female *Macaca mulatta* and *Macaca fascicularis*, aged 10–12 years, acquired using a 3T system with the MP2RAGE sequence. **4) Stem Cell and Brain Research Institute:** includes 22 scans from 9 male and 13 female *Macaca mulatta* and *Macaca fascicularis*, aged 3.6–14 years, acquired using 1.5T and 3T systems with the MPRAGE sequence. **5) University of California, Davis:** includes 19 scans from 19 female *Macaca mulatta*, aged 18.5–22.5 years, acquired using a 3T system with the MPRAGE sequence.

For consistency with the challenge dataset, a similar preprocessing pipeline was applied to the zero-shot datasets. This included skull-stripping, affine registration to a  $1 \times 1 \times 1$  mm MNI template [56], and bias field correction using ANTS [57]. Because the macaque brain images were originally acquired at a resolution of  $1 \times 1 \times 1$  mm but were significantly smaller than human brains, we scaled them up by a factor of 1.5. To ensure proper affine alignment, a macaque brain was first affinely registered to the MNI template and qualitatively evaluated; all remaining macaque brains were subsequently aligned to this initial macaque image. T1-weighted MRI scans from human participants

were segmented into 133 cortical and subcortical anatomical structures using SLANT [48]. The resulting label maps were propagated from T1-weighted scans to T2\*-weighted and FLAIR scans. For non-human primates (ie., macaques), brain segmentation was performed using nBEST [58], an automated method that delineates nine anatomical structures. The resulting label maps from the segmentation algorithms were reviewed by the challenge organizers, who have extensive experience in neuroimaging research.

## 4.2 Comparisons

We compute a range of comparisons to evaluate registration performance that assess the accuracy, robustness, plausibility, and speed of the algorithms. We specifically use the following:

- **DSC:** The Dice similarity coefficient (DSC) [59] measures the overlap of two sets of segmentation labels. The DSC provides a reference for the general accuracy of the methods, although it has limitations [60] specifically related to registration evaluation [14].
- **DSC30:** To assess robustness, DSC30 considers the 30<sup>th</sup> percentile of DSC scores on all anatomical structures and cases. It serves to identify the worst-case scenarios for the methods with respect to the DSC.
- **HD95:** The Hausdorff distance (HD) [61] indicates the maximum distance in a metric space between two sets, in this case segmentation labels of the fixed and warped moving images. For a robust score, it is customary to consider the 95<sup>th</sup> (HD95) percentile instead of the maximum distance.

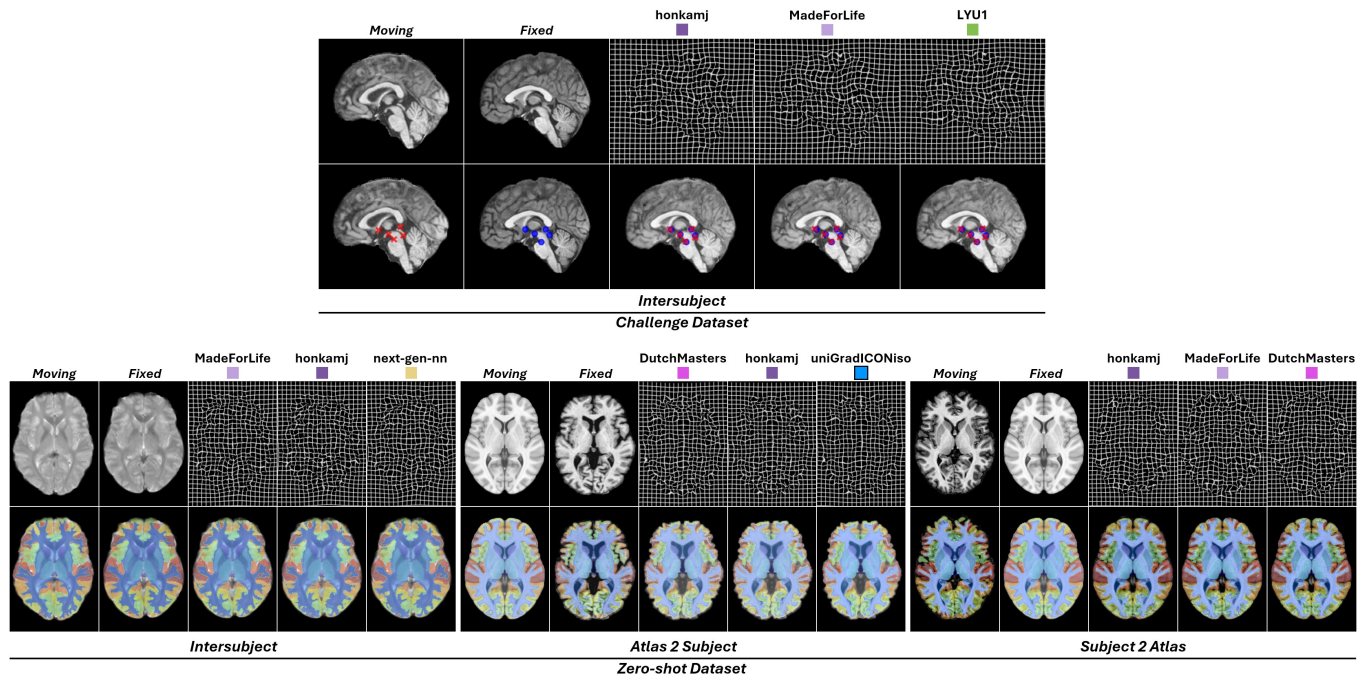


Fig. 3. Representative registration results from the challenge and zero-shot evaluation tasks. The top panel shows results on the challenge dataset, including moving and fixed images, deformation fields, deformed moving images from the top three methods (selected from Fig. 1 and shown left to right in rank order), and the corresponding anatomical landmarks. The bottom panel presents results from three zero-shot generalization tasks: intersubject, atlas-to-subject, and subject-to-atlas registration. For each task, the top three methods (also ranked left to right) are shown with their respective deformation grids and propagated anatomical label maps.

- **TRE**: The target registration error (TRE) is defined as the Euclidean distance between the corresponding landmarks in the fixed and warped moving images.
- **TRE30**: Similarly to the DSC30 score, the TRE30 reports the 30<sup>th</sup> percentile of the largest distances from the landmark.
- **NDV**: The non-diffeomorphic volume (NDV) [29] quantifies the size of the non-diffeomorphic space in 3D caused by a digital transformation. It avoids the incorrect estimation arising from the central differences based Jacobian determinant computation by computing the volume of folded space in 3D.
- **ACC**: To provide a summary statistic of registration accuracy (ACC), we pool the rankings of DSC, HD95, and TRE (when available).
- **Runtime**: The average runtime of each method is computed from ten repeated measurements performed on CPU, including image I/O operations. This ensures fair comparisons with traditional optimization-based methods, which typically have CPU-only implementations.

In line with previous editions of the Learn2Reg Challenge [6], which followed the standard set by the Medical Decathlon [5], we rank the methods using the Wilcoxon signed-rank test. Specifically for each of DSC, HD95, TRE, and NDV, all methods are compared against each other using the paired Wilcoxon signed rank test with a one-sided alternative hypothesis, a per comparison  $\alpha = 0.05$ , and no adjustment for multiple comparisons. The ranking for DSC, HD95, TRE, and NDV, is then determined based on the number of comparisons a method “won”, with the

number of wins for each method assigned to values between 0.1 and 1 with the possibility of multiple methods having the same rank. Finally, a task rank score is obtained by taking the geometric mean of the individual rank scores. An almost identical procedure is used to rank the methods based on their DSC30 and TRE30, with the modification that an unpaired Wilcoxon rank-sum test (Mann–Whitney U test) is used. The unpaired test is used, as the 30<sup>th</sup> percentile of data represented in the DSC30 or TRE30 is different between methods. The rankings for each of the methods across the challenge test set and zero-shot evaluations are reported in Fig. 1. The summary results for each of the evaluations for the challenge test set are presented in Table 1.

### 4.3 LUMIR Challenge Setup

The LUMIR challenge consisted of three phases (mainly organized on grand-challenge.org).

- **Phase 1 – Validation Phase**: The challenge began on April 1<sup>st</sup>, 2024, allowing participants to download the training and validation datasets and train their registration networks using the training images. Participants then generated displacement fields for the validation cases, which were subsequently submitted and automatically evaluated via grand-challenge.org. Participants whose submissions ranked within the top 10 on the leaderboard were invited to provide method descriptions by June 24<sup>th</sup>, 2024, and present posters at the Workshop on Biomedical Image Registration (WBIR), held during the 27<sup>th</sup> International Conference on Medical Im-

age Computing and Computer Assisted Intervention (MICCAI 2024).

- **Phase 2 – Test phase:** After the validation phase, participants had until September 8<sup>th</sup>, 2024 to submit a Docker container to the organizers. This container included their registration models in executable form, designed to read input image pairs from a provided file listing all test set pairs, and subsequently generate the corresponding displacement fields. The organizers evaluated these displacement fields using both label maps and anatomical landmarks. The performance metrics and final rankings were then computed and presented at the MICCAI conference.
- **Phase 3 – Further analysis phase:** After the challenge concluded at MICCAI 2024, the organizers conducted further analyses of the submitted algorithms by evaluating their zero-shot performance on out-of-domain datasets, whose data distributions differed from those used during training. The results and findings of this analysis are summarized in this paper.

The LUMIR challenge attracted a total of 39 participants across 31 teams, each submitting at least one set of computed displacement fields during the validation phase. Collectively, these participants contributed 247 valid entries to the challenge leaderboard. In the subsequent test phase, 12 teams submitted their trained models for evaluation. Notably, while one team consisted of industry professionals, the remaining teams were affiliated with academic institutions.

#### 4.4 Participating Methods

#### 4.5 Submissions

We summarize all evaluated registration methods in Table 4, highlighting their image similarity metrics, deformation regularization techniques, model design choices, runtime, and availability as open-source models. For comprehensive descriptions of image similarity metrics and deformation regularization methods, readers are referred to a recent survey [15]. The main architectural design choices listed in the table are defined as follows:

- **Dual-Stream Encoders:** Two separate encoders extracting features from moving and fixed images, which may either share weights or be trained independently.
- **Coarse-to-Fine Pyramid:** Models (either deep learning- or optimization-based) that generate deformation fields or perform registration in a coarse-to-fine manner. Note that this is distinct from whether the underlying network employs multi-resolution architectures.
- **Progressive Registration:** Models that progressively refine deformation fields. For deep learning methods, this involves using multi-stage networks, with each subsequent network refining the deformation produced by the previous stage. For optimization-based methods, progressive refinement is inherently built-in, as each iteration updates and improves the deformation estimate.
- **Cost Volume:** Computation of a cost volume containing similarity or distance measures (e.g., correlation or Euclidean distance) between intensity or feature values at corresponding voxels or patches in the fixed and moving images.
- **Attention:** Models incorporating attention mechanisms (e.g., self-attention, cross-attention, or other variants) within their architectures.
- **Inverse Consistency by Construction:** Models explicitly designed to guarantee inverse consistency, such that the forward deformation  $\phi_{A \rightarrow B}$  is the inverse of the backward deformation  $\phi_{B \rightarrow A}$ . In deep learning-based methods, this is often achieved by exponentiating the difference between intermediate fields computed by an auxiliary network [30]; in optimization-based approaches, symmetric optimization schemes are used, as in [18].
- **Diffeomorphic Registration:** Models that employ formulations (e.g., time-varying velocity fields or stationary velocity fields) to achieve diffeomorphic (smooth, invertible) deformation fields.
- **Instance-Specific Optimization:** Models that iteratively refine deformation fields for each specific image pair by optimizing the registration objective function individually per instance.

Following this overview, we introduce each method individually using a concise three-line summary: the first line includes a colored square (that is used in plots and figures for quick reference) and the name of the method; second is a one line summary of the method; and finally in parentheses is the Participant(s) that contributed the method. Each summary is then followed by a brief description of the respective method.

#### ■ Bailiang

*Dual-stream encoders, coarse-to-fine pyramid, correlation layers, and progressive registration*  
(Bailiang Jian & Benedikt Wiestler [62])

Bailiang ■ introduces a ConvNet architecture designed with registration-specific components. It employs dual-stream encoders to independently extract image features from moving and fixed images, followed by a decoder that integrates these features with a coarse-to-fine optimization pyramid to progressively refine deformations across scales. The network also employs progressive registration to iteratively compose deformation fields to enable large deformations, while correlation layers establish voxel-wise correspondences.

#### ■ next-gen-nn

*Robust backbone network*  
(Yuxi Zhang & Hang Zhang)

next-gen-nn ■ uses a robust backbone network based on Zhang *et al.* [63]. Their network architecture comprises an encoder with a series of convolutional layers and a cascaded mechanism designed to refine the prediction of deformation fields. Specifically, next-gen-nn ■ uses modifications to the base network, including a co-attention mechanism [64], large kernel convolutions [65], and an increased number

TABLE 4

Overview of the 21 registration methods evaluated in the LUMIR challenge. The image similarity measures, regularization terms used in the registration formulation, and model design choices for each method are marked with a ●. For diffeomorphic registration, methods that do not mathematically guarantee diffeomorphisms but adopt alternative formulations that approximate them are denoted by ○. The average runtime per image pair (measured on CPU) and the public availability of the source code are also provided. Note that the runtime for `zhuoyuanw210` is omitted, as the implementation requires a GPU and cannot be fairly compared with CPU-only methods.

	Similarity			Regularizer							Model Design						Run Time (CPU)	Open Source
	NCC	MIND-SSC	Dice	Diffusion	Inverse Consist.	Jacobian Det.	Kinetic Energy	Gaussian Smooth.	Dual-Stream Enc.	Coarse-to-Fine	Progressive Reg.	Cost Volume	Attention	IC by Construction	Diffeomorphic Reg.	Instance-spec. Opt.		
BaiIiang	●			●					●	●	●	●					14.93s	🔗
next-gen-nn	●			●						●	●		●				16.50s	
honkamj	●			●						●	●	●		●	●		51.70s	🔗
LoRA-FT	●				●					●	●	●		○	●		18.20s	
MadeForLife	●			●						●	●	●	●		●		8.79s	
lukasf	●			●							●		●				4.62s	
LYU1	●			●						●	●		●				15.86s	
TimH	●					●								●	●		9.41s	🔗
VROC	●							●			●				●		152.70s	🔗
DutchMasters	●				●					●	●			○	●		1458.44s	
zhuoyuanw210	●			●						●	●		●				-	
ANTs SyN	●						●			●	●			●	●	●	988.70s	🔗
deedsBCV		●		●						●	●	●			●	●	43.34s	🔗
FireANTs Greedy	●							●		●	●			●	●	●	61.24s	🔗
FireANTs SyN	●						●			●	●			●	●	●	2289.42s	🔗
SynthMorph			●	●										●			28.62s	🔗
TransMorph	●			●							●	●					8.00s	🔗
uniGradICON	●				●					●	●			○			16.69s	🔗
uniGradICON w/ ISO	●				●					●	●			○	●		1265.90s	🔗
VFA	●			●						●		●					13.97s	🔗
VoxelMorph	●			●						●	●						4.11s	🔗

of convolutional channels in the prediction stage of the deformation field. Additionally, `next-gen-nn` uses an image-guided bilateral filtering technique [66], to refine the predicted registration results.

### ■ honkamj

*Symmetric, inverse consistent, and topology preserving by construction*

(Joel Honkamaa & Pekka Marttinen [67])

`honkamj` is a novel multi-resolution deep learning registration architecture which is inverse consistent, symmetric, and preserves topology by construction. These properties are fulfilled for the whole multi-resolution pipeline and not just separately at each resolution.

`honkamj` is designed to be cycle-consistent. That means that the deformation field,  $f$ , between two images  $A$  and  $B$  is  $f(A, B)$  and we want the composition of  $f(A, B)$  and  $f(B, A)$  to be the identity. The authors achieve this goal through a clever trick of setting up an auxiliary network  $u$  that predicts deformations and defines  $f$  as  $f(A, B) = u(A, B) \circ u(B, A)^{-1}$ . By construction, the authors have  $f(A, B) = f(B, A)^{-1}$ , up to numerical precision. This approach of using an intermediate network and creating the desired deformation field through an inverse consistent construction has been previously proposed by Estienne *et al.* [68]. Inverse consistency is not guaranteed by Estienne *et al.* as they enforce it via a loss term, whereas the formulation

of `honkamj` is symmetric by construction. To implement this inverse consistent approach effectively, the authors encode features of the inputs separately before feeding them to the deformation extraction network  $u$ .

The approach is implemented in a multi-scale manner; from the lowest resolution, features are extracted and used to create the coarsest deformation field. Then the approach recursively builds deformations between the inputs at each level using the extracted features. To ensure symmetry, two deformations are built: one deforming the first image half-way towards the second image, and the other deforming the second image half-way towards the first image. The final deformation is the composition of these two deformations at the highest resolution level. For more details, see Honkamaa and Marttinen [67]; we note that the model trained for the challenge used the group consistency loss over image triplets [69].

### ■ LoRA-FT

*Low-rank adaptation of foundation models*

(Jin Kim & Matthew S. Brown)

Adapting `uniGradICON` [28] foundation models to new domains or datasets typically requires extensive fine-tuning of millions of parameters, which is computationally expensive and can lead to catastrophic forgetting. `LoRA-FT` addresses this limitation by using Low-rank

Adaptation (LoRA) [70] to achieve parameter-efficient adaptation. Rather than fine-tuning all network parameters, `LoRA-FT` ■ decomposes weight updates into low-rank matrices, reducing the number of trainable parameters by orders of magnitude while maintaining registration performance. The approach enables rapid adaptation of the foundation model to any dataset without compromising its general registration capabilities or requiring direct supervision of anatomical label maps.

### ■ MadeForLife

*Dual-stream encoders with a specialized decoder for coarse-to-fine pyramid and progressive registration*  
(Yichao Zhou & Zuopeng Tan)

The authors use the GroupMorph [71] structure for their approach. Using a dual encoder with shared weights to extract multilevel features for both the fixed and moving images. The encoder adopts a structure similar to that of `VoxelMorph` □ [72]. The features extracted by the dual encoder are fed into grouping update modules (GUMs) for the production of deformation fields and contextual features, where the contextual features provide explicit prior information and intergroup correspondence for the generation of the deformation field. The GUMs consist of two parts: the grouping module (GM), which calculates feature correlation and generates deformation fields, and the contextual fusion module (CFM), which fuses contextual features to facilitate inter-group communication for the grouping field estimator.

In summary, GMs use a different number of convolutional layers to compute multiple deformation subfields per level, with these subfields having different receptive fields. The intralevel multiscale fields, along with the interlevel multiscale fields, form the final deformation fields. Compared to the manner of predicting one field per level, the finer grained decomposing can further promote model optimization, thereby obtaining an optimal alignment. The CFMs facilitate collaboration among subfields within each group, the CFMs fuse the contextual features from adjacent groups, thus their intergroup communication is strengthened. This enables every group to have access to explicit prior information from the other groups while estimating the deformation fields.

### ■ lukasf

*TransMorph refinement*

(Lukas Förner & Thomas Wendler)

The authors propose a fine-tuning of a pre-trained `TransMorph` ■ [73] model to improve convergence stability and deformation smoothness. Convergence stability is achieved through the Fisher Adam (FAdam) [74] optimizer, and the deformation smoothness comes from the addition of gradient correlation [75] in the similarity measure, which improves anatomical alignment. The results show slight improvements in the Dice and HD95 scores, and a notable reduction in the NDV compared to the baseline `TransMorph` ■ model.

The authors use the FAdam optimizer to improve optimization during training. FAdam is a variant of the Adam optimizer that incorporates principles from natural gradient descent and Riemannian geometry to improve convergence

and stability. The key modifications in FAdam include adjustments to momentum, bias correction, adaptive gradient scaling, and a refined weight decay that respects the geometry of the parameter space. `lukasf` ■ also incorporates the gradient correlation [75] in their loss computation along with the local normalized cross-correlation, as part of the similarity loss between the fixed and moving images.

### ■ LYU1

*Pyramid network with auxiliary decoder*

(Hongchao Zhou & Shunbo Hu)

`LYU1` ■ proposes a shared encoder, a shared auxiliary decoder, and a fusion pyramid decoder. The fusion pyramid decoder includes five scales. Except for the smallest scale, each scale is constructed from a multi-scale feature fusion block (MSFB). The pyramid decoder first merges the smallest-scale low-level features and predicts a coarse deformation field. This deformation field is then upsampled and applied to the moving feature map at the current scale. The moving feature map, the fixed feature map, and the high-level moving and fixed features from the shared auxiliary decoder at the same scale are input into the MSFB. This process removes redundant information and produces fused features, predicting the deformation field at the current scale. This process is repeated at each scale, with the final refined deformation field obtained by iteratively combining the coarse deformation fields from each scale.

### ■ TimH

*ConstrICON framework multistep inverse consistency*

(Tim Hable)

This approach addresses the challenge of unsupervised registration of anatomical structures in brain MRI by using the ConstrICON framework [76], which is used to build an inverse consistent multistep registration model. The approach employs residual U-Nets and applies additional smoothing to the stationary velocity fields to reduce the inverse consistency error.

The approach leverages the *TwoStepConsistent* (TSC) operator from the ConstrICON framework. In contrast to other approaches, that utilize penalty terms during training to approximate inverse consistency, ConstrICON achieves this property intrinsically through its architectural design and by parameterizing the output transformations of the neural networks by a Lie group. Parameterizing the output of a neural network by a Lie group is assumed to be sufficient, since many types of transformations that are used in medical image registration, such as affine or diffeomorphic transforms, are Lie groups. The TSC operator preserves inverse consistency by construction—see Greer *et al.* [76] for complete details—and can be recursively applied, thereby extending the procedure from a two-step registration to an  $N$ -step approach that remains inverse consistent. The proposed model uses three residual U-Nets, denoted as  $\Xi$ ,  $\Phi$ , and  $\Psi$ , to construct a three-step inverse consistent framework of the form  $TSC\{\Xi, TSC\{\Phi, \Psi\}\}$ . Within each TSC operator (e.g.,  $TSC\{\Phi, \Psi\}$ ), the network  $\Phi$  is constrained to learn only the square root of the transformation, while  $\Psi$  learns the full transformation. The stationary velocity field is smoothed via average pooling (kernel size 3, applied

twice), which empirically reduces inverse consistency error. Each registration network also includes selective Jacobian determinant regularization [77] to mitigate folding. The final output of the combined registration networks is regularized using bending energy loss [78] and selective Jacobian determinant regularization loss, with NCC as the similarity metric.

### ■ VROC

*Variational Registration on Crack*

(Frederic Madesta & Thilo Sentker)

The Variational Registration on Crack (VROC ■) toolbox employs a classic registration approach using task-specific hyperparameters and image preprocessing steps to improve performance. For the LUMIR Challenge the pre-processing includes Gaussian smoothing with a  $\sigma$  of 1 to reduce the noise. Intensity-based label maps are generated using a multi-Otsu thresholding with seven classes. A registration mask is created by taking the union of the fixed and moving images where pixel values are greater than zero, ensuring that only relevant regions are considered during the registration process. Deformable registration is performed for the first time using NCC forces applied to the fixed and moving label maps based on thresholds. This is followed by fine-tuning the initial registration result with Demons forces [79] (on the original intensity-based images) to achieve precise alignment and handle more complex deformations.

### ■ DutchMasters

*Gradient projection optimization*

(Yi Zhang & Qian Tao [80])

DutchMasters ■ introduces a novel instance optimization (IO) algorithm that addresses the multi-objective optimization (MOO) challenge that is inherent to image registration. The approach applies gradient projection techniques, inspired by advances in MOO [81], to enhance the effectiveness of IO. IO effectively combines the generalization capabilities of deep learning with the fine-tuning advantages of instance-specific optimization. The authors framework uses gradient projection to mitigate conflicting updates in the MOO. The technique projects conflicting gradients into a common space, better aligning the dual objectives and enhancing optimization stability. The authors consider the components of the loss being optimized (i.e. similarity and regularization) as components in a MOO. The multiple losses can sometimes be in conflict with each other, affecting the optimization which is reflected in the direction and magnitude of the loss gradients. DutchMasters ■ address this by using the gradient projection technique from multi-task learning [81]. The conflicting direction of the loss gradients is corrected by randomly projecting one gradient to the normal space of the other. Conflicting gradients are identified by evaluating the cosine similarity between two gradients. Unlike mini-batch calculation [81], the authors focus on instance optimization, thus reducing the scope from multi-task learning to multi-objective optimization. If the gradients are not conflicting, the update will remain unchanged compared to gradient-based methods. If, however, the gradients are in conflict, one of the gradients will be randomly projected to the normal space of the other, and

that gradient will be used for the update. For complete details, see Zhang *et al.* [80].

### ■ zhuoyuanw210

*Dual stream pyramid encoder and motion decomposition transformer*

(Zhuoyuan Wang & Yi Wang)

This method employs a dual-stream pyramid encoder and a GPU-accelerated motion decomposition Transformer (ModeTv2) [82] decoder. The dual-stream pyramid encoder extracts features from both the moving image and the fixed image, generating corresponding feature hierarchies for each image. The feature hierarchies are used from coarse to fine to generate deformations between the moving and fixed image at each scale level.

## 4.6 Baseline Methods

For each of the Baseline methods we also provide a three line summary: the first line includes a colored square (that is used in plots and figures for quick reference) and the name of the method; second is a one line summary of the method; and finally in parentheses is the reference for the method. Following the one line summaries is a brief overview of the respective methods and Table 4 includes additional details about the methods.

### □ ANTSyN

*Optimization-based, symmetric, time-varying diffeomorphic registration*

(Avants *et al.* [18], [83], [84])

Originally proposed circa 2007 [18], [83], the symmetric image normalization method (SyN), now packaged as part of the Advanced Normalization Tools (ANTs), is a traditional registration framework that maximizes the cross-correlation (CC) within the space of diffeomorphic maps using Euler-Lagrange equations during optimization.

The approach was the first to use CC for diffeomorphic registration, and their CC normalization formulation allowed for symmetrizing the cross-correlation of the Euler-Lagrange equations, while only incurring a minor additional computational cost. It works by iteratively applying transformations to align the images in a symmetric manner, thus optimizing the transformation in both directions simultaneously. The symmetry used in ANTSyN □ ensures that the transformation is optimal in both directions, which removes bias from the directionality of the transformation. ANTSyN coming from the pre-deep learning era can be computationally expensive, which is often reported as a criticism despite its continued good results on a wide range of imaging data and organs [1], [85], [86].

### ■ deedsBCV

*Optimization-based, discrete registration*

(Mattias *et al.* [87])

deedsBCV ■ was designed to address three outstanding issues of lung CT registration: large motion of small features, sliding motions between organs, and changes in image contrast due to compression. The approach takes advantage of Markov random field (MRF)-based discrete

optimization strategies while also keeping computational complexity tractable without reducing the registration accuracy.

deedsBCV [10] made three distinct contributions, first the use of an image-derived minimum spanning tree as a simplified graph structure to handle the complexity of sliding motion and allowed for the estimation of the global optimum very efficiently. Secondly, a stochastic sampling approach for the similarity cost between images is introduced within a symmetric, diffeomorphic B-spline transformation model with diffusion regularization. This helps reduce the complexity of the computation by orders of magnitude and enables the minimization of much larger label spaces. Thirdly, the addition of proxy-labels, dubbed hyper-labels, are introduced which capture the local intensity variations arising within this task. deedsBCV [10] was originally designed for lung CT registration; however, it has been shown to be quite adapt at a broad range of tasks [6].

### ■ FireANTsGreedy / ■ FireANTsSyN

*Optimization-based, GPU-accelerated, time-varying diffeomorphic registration*

(Jena et al. [88])

Traditional registration algorithms such as ANTsSyN [18], [83] have endured over the years due to their precision, reliability, and robustness in a wide spectrum of modalities and acquisition settings. However, these algorithms converge slowly, are prohibitively expensive to run, and their usage requires a steep learning curve, limiting their scalability to larger clinical and scientific studies. The authors of the FireANTs approach have developed a multiscale adaptive Riemannian optimization algorithm for diffeomorphic image registration. Their framework leverages mathematical correspondences to avoid expensive operations like the Riemannian metric tensor, and parallel transport of the optimization state, which are needed for implementing first-order adaptive algorithms. FireANTs can compose transformations, avoiding resampling artifacts across transformations. All of this with the aim of improving scalability in image registration.

### ■ SynthMorph

*Learning contrast-agnostic registration without acquired images*

(Hoffmann et al. [16])

SynthMorph [16] is a general strategy for learning contrast-agnostic registration. SynthMorph [16] enables the registration of real images within and between contrasts, learning only from synthetic data. During training, SynthMorph [16] synthesizes images from label maps and trains the registration framework to align these synthetic images. The approach uses a generative model to provide random label maps of variable geometric shapes. Conditioned on these generated label maps, they synthesize images with arbitrary contrasts, deformations, and artifacts. SynthMorph [16] can then train with a contrast-agnostic loss that measures label overlap, rather than an image-based loss.

### ■ TransMorph

*Vision Transformer-based registration model*

(Chen et al. [73])

TransMorph [73] is a deep learning-based image registration framework that incorporates a Transformer-based architecture for both affine and deformable registration. Its encoder consists of a three-stage Swin Transformer [89], which extracts hierarchical features from the input images. These features are then passed to a decoder that progressively refines the deformation field, composing each new estimate with the previously generated field [90]. TransMorph [73] is trained using an unsupervised learning paradigm similar to that of VoxelMorph [19], with both fully unsupervised and semi-supervised variants (leveraging anatomical label maps during training) described in the literature.

### ■ uniGradICON / ■ uniGradICONiso

*Inverse consistent, learning-based foundation registration model*

(Tian et al. [28])

The authors propose to train a universal foundation model for registration. A hurdle to developing a foundation model for registration is the obstacle of training a universal registration network over many different datasets to obtain such a model. It is incredibly difficult to pick a set of registration hyperparameters (for regularizers and similarity measures) that provide good performance across a wide-range of registration tasks. The issue of different registration tasks requiring different hyperparameters is obviously in direct conflict with a universal registration network being trained with a fixed set of hyperparameters. However, this is made possible by replacing conventional regularizers with gradient inverse consistency (*GradICON*) regularization [31]. *GradICON* acts as a weak regularizer that only encourages invertibility of the transform. This weak constraint, allows the network to discover what transformations are supported by the data and thereby facilitates training with the same hyperparameters across different datasets. The uniGradICONiso version incorporates instance-specific optimization, iteratively fine-tuning the network parameters for 50 iterations for each image pair.

### ■ VFA

*Dual-stream encoders, vector field cross-attention decoder, multi-scale registration model*

(Liu et al. [91])

Vector field attention (VFA [91]) is an extension of the previously published *im2grid* [92]. VFA uses neural networks to extract multiresolution feature maps from the fixed and moving images and then retrieves pixel-level correspondences based on feature similarity. Retrieval of the correspondences is achieved with a novel attention module without the need for learnable parameters. VFA is trained end-to-end in either a supervised or unsupervised manner.

### ■ VoxelMorph

*U-Net-based registration model*

(Balakrishnan et al. [19])

VoxelMorph [19] is a fast learning-based framework for deformable, pairwise medical image registration. In contrast

to traditional registration methods, `VoxelMorph` is formulated as a function that maps an input image pair to a deformation field that aligns the input images. The underlying network is parameterized by CNNs. Both supervised and unsupervised versions have been reported in the literature.

## 5 CONCLUSION

The LUMIR challenge has highlighted the transformative impact of deep learning on brain MRI image registration, by presenting both promising insights and remaining challenges. From our comprehensive experiments and comparisons, we demonstrate that deep learning-based registration methods significantly outperform traditional optimization-based approaches in inter-subject and atlas-based brain MRI registration.

The LUMIR challenge datasets are characterized by two major focuses: their large-scale and unsupervised nature. By incorporating datasets with substantial distributional variations relative to the training data (i.e., T1-w images of healthy adult brains), the challenge establishes a rigorous benchmark for assessing model robustness and adaptability. This includes differing variations in modalities, anatomies, and even species. The inclusion of datasets such as ADHD, ADNI1.5T, ADNI3T, NIMH, and UltraCortex offers a broad spectrum of neuroimaging scenarios, ensuring that models are evaluated across a range of realistic clinical conditions. Additionally, the unsupervised nature of the LUMIR challenge is important in advancing registration technology. By deliberately excluding label maps from training, the challenge shifts focus toward achieving registration accuracy and deformation smoothness through unsupervised methods. This encourages the development of models that inherently learn spatial correspondences and adapt to diverse data conditions without relying on predefined labels, further promoting the creation of generalizable and scalable registration solutions. This framework also fosters innovation in the development of foundational models that can operate effectively in environments where annotated data is scarce.

In Sec. 3, we provided comprehensive insights into the promising advancements and remaining challenges of various deformable registration approaches. Our evaluation of zero-shot registration revealed that deep learning models consistently outperform traditional optimization-based techniques, even in scenarios with substantial domain shifts, such as differing contrasts, anatomical pathological changes, and species variations. This success demonstrates the maturity of deep learning methods and suggests these models possess strong generalization capabilities when provided with sufficient training data. Furthermore, architectural choices, like dual-stream encoders, are important in achieving effective registration performance. This indicates that thoughtful model design could be a promising avenue for future improvements.

Contrary to traditional views, our findings demonstrate that deformation regularity can coexist with high registration accuracy, facilitated by innovative model designs. Additionally, while instance-specific optimization can sometimes enhance performance, single-step approaches are more efficient in producing smooth deformations without added

computational complexity. However, achieving perfect inverse consistency remains challenging, with models experiencing minor deviations due to interpolation errors despite being designed to ensure consistency. Finally, our analysis showed a poor correlation between DSC and TRE, highlighting the need for careful evaluation design in future registration challenges. Collectively, these insights from the LUMIR challenge advance our understanding of medical image registration and guide future research directions in model development and optimization.

In conclusion, the LUMIR challenge embodies the ongoing advancements of medical image registration, leveraging the advancements of deep learning to address its fundamental role in clinical applications. We moved beyond the constraints of anatomical label map supervision, and encourage the models to produce smooth and realistic deformations. These efforts not only enhance registration accuracy and efficiency but also broaden the scope of applicability across different anatomical contexts. Through extensive evaluations and discussions, LUMIR challenge gave us valuable insights and highlight potential directions for future improvements. As the field progresses, we believe LUMIR will play an important role in shaping the future of medical image registration, ultimately unlocking new possibilities for clinical and research advancements.

## APPENDIX ADHD

TABLE A1  
ADHD Inter-subject.

Method	DSC		HD95		Ranking (ACC)	NDV		DSC30	
	Mean(±Std. Dev)	Mean(±Std. Dev)	Mean(±Std. Dev)	Mean(±Std. Dev)		Mean(±Std. Dev)	Mean(±Std. Dev)		
Balliang	0.767(±0.017)	3.357(±0.470)	3	2.98e-02(±9.51e-03)	7	0.745(±0.007)			
next-gen-nn	0.769(±0.018)	3.330(±0.479)	2	2.73e-04(±2.16e-04)	7	0.747(±0.006)			
honkamj	0.778(±0.017)	3.048(±0.451)	1	2.26e-03(±3.58e-04)	5	0.755(±0.005)			
LoRA-FT	0.742(±0.021)	3.651(±0.461)	18	1.64e-03(±1.98e-03)	10	0.714(±0.006)			
MadeForLife	0.773(±0.017)	3.281(±0.475)	3	7.11e-03(±2.99e-03)	3	0.751(±0.007)			
lukasz	0.762(±0.016)	3.417(±0.443)	5	2.09e-01(±3.94e-02)	6	0.741(±0.006)			
LYU1	0.770(±0.016)	3.286(±0.437)	4	1.23e-02(±1.47e-03)	6	0.750(±0.006)			
TimH	0.733(±0.017)	3.699(±0.441)	17	0.00e+00(±0.00e+00)	10	0.712(±0.009)			
VROC	0.749(±0.023)	3.698(±0.484)	14	4.16e-02(±2.00e-02)	10	0.719(±0.008)			
DutchMasters	0.767(±0.019)	3.253(±0.461)	4	1.93e-03(±8.37e-04)	4	0.743(±0.008)			
zhuoyuanw210	0.768(±0.015)	3.230(±0.425)	5	2.98e-03(±6.74e-04)	4	0.749(±0.006)			
ANTeSyN	0.734(±0.022)	3.483(±0.450)	13	0.00e+00(±0.00e+00)	10	0.706(±0.011)			
DeedsBCV	0.696(±0.019)	4.083(±0.447)	21	8.22e-05(±1.55e-04)	4	0.672(±0.010)			
FireANTsGreedy	0.750(±0.018)	3.649(±0.456)	16	0.00e+00(±0.00e+00)	10	0.726(±0.007)			
FireANTsSyN	0.747(±0.019)	3.682(±0.457)	16	1.33e-05(±8.18e-06)	10	0.723(±0.008)			
SynthMorph	0.725(±0.017)	3.584(±0.429)	10	6.52e-06(±7.66e-06)	10	0.704(±0.005)			
TransMorph	0.758(±0.018)	3.460(±0.444)	11	3.13e-01(±5.03e-02)	10	0.736(±0.005)			
uniGradICON	0.747(±0.021)	3.519(±0.472)	12	4.52e-05(±3.33e-05)	10	0.719(±0.007)			
uniGradICONiso	0.736(±0.018)	3.425(±0.384)	10	5.65e-05(±3.67e-05)	10	0.733(±0.007)			
VFA	0.773(±0.015)	3.323(±0.439)	6	5.88e-02(±1.99e-02)	6	0.754(±0.005)			
VoxelMorph	0.715(±0.024)	4.029(±0.457)	23	1.16e+00(±1.39e+01)	6	0.685(±0.014)			
ZeroDisplacement	0.582(±0.029)	4.832(±0.481)	22	0.00e+00(±0.00e+00)	10	0.549(±0.019)			

TABLE A2  
ADHD Atlas to Subject.

Method	DSC		HD95		Ranking (ACC)	NDV		DSC30	
	Mean(±Std. Dev)	Mean(±Std. Dev)	Mean(±Std. Dev)	Mean(±Std. Dev)		Mean(±Std. Dev)	Mean(±Std. Dev)		
Balliang	0.745(±0.013)	3.458(±0.352)	11	2.98e-02(±4.43e-03)	7	0.730(±0.007)			
next-gen-nn	0.750(±0.013)	3.410(±0.369)	9	1.72e-04(±1.78e-04)	7	0.734(±0.007)			
honkamj	0.764(±0.012)	3.132(±0.342)	1	7.74e-04(±1.95e-04)	5	0.751(±0.007)			
LoRA-FT	0.740(±0.013)	3.395(±0.384)	10	3.16e-03(±1.48e-03)	10	0.725(±0.008)			
MadeForLife	0.755(±0.013)	3.330(±0.356)	8	2.87e-03(±1.11e-03)	6	0.740(±0.006)			
lukasz	0.742(±0.013)	3.453(±0.369)	9	2.48e-01(±4.07e-02)	6	0.727(±0.008)			
LYU1	0.748(±0.013)	3.333(±0.369)	7	1.30e-02(±2.38e-03)	6	0.732(±0.007)			
TimH	0.719(±0.013)	3.569(±0.359)	18	0.00e+00(±0.00e+00)	10	0.704(±0.007)			
VROC	0.707(±0.014)	3.749(±0.336)	20	7.43e-02(±2.40e-02)	10	0.690(±0.009)			
DutchMasters	0.763(±0.012)	3.174(±0.377)	2	1.34e-03(±6.08e-04)	4	0.748(±0.008)			
zhuoyuanw210	0.759(±0.011)	3.246(±0.354)	3	2.24e-03(±3.50e-04)	4	0.745(±0.006)			
ANTeSyN	0.745(±0.013)	3.351(±0.365)	8	0.00e+00(±0.00e+00)	10	0.731(±0.007)			
DeedsBCV	0.698(±0.016)	3.732(±0.371)	21	2.70e-04(±4.69e-04)	4	0.679(±0.008)			
FireANTsGreedy	0.745(±0.013)	3.475(±0.382)	12	0.00e+00(±0.00e+00)	10	0.730(±0.007)			
FireANTsSyN	0.745(±0.015)	3.442(±0.397)	10	1.57e-05(±1.30e-05)	10	0.729(±0.009)			
SynthMorph	0.722(±0.019)	3.457(±0.398)	16	1.00e-05(±1.04e-05)	10	0.702(±0.007)			
TransMorph	0.735(±0.012)	3.514(±0.363)	13	3.48e-01(±4.92e-02)	10	0.721(±0.006)			
uniGradICON	0.739(±0.012)	3.371(±0.371)	11	2.74e-05(±2.55e-05)	10	0.725(±0.007)			
uniGradICONiso	0.754(±0.011)	3.239(±0.354)	4	3.55e-05(±3.93e-05)	10	0.741(±0.007)			
VFA	0.750(±0.013)	3.271(±0.344)	6	5.07e-02(±1.56e-02)	6	0.736(±0.007)			
VoxelMorph	0.717(±0.018)	3.731(±0.444)	19	1.17e+00(±1.33e+01)	6	0.696(±0.010)			
ZeroDisplacement	0.569(±0.031)	4.590(±0.518)	22	0.00e+00(±0.00e+00)	10	0.534(±0.015)			

TABLE A3  
ADHD Subject to Atlas.

Method	DSC	HD95	Ranking	NDV	DSC30
	Mean( $\pm$ Std. Dev.)	Mean( $\pm$ Std. Dev.)	(ACC)	Mean( $\pm$ Std. Dev.)	Mean( $\pm$ Std. Dev.)
Bailling	0.774( $\pm$ 0.011)	3.127( $\pm$ 0.385)	1	7.61e-03( $\pm$ 2.46e-03)	0.762( $\pm$ 0.007)
next-gen-nn	0.772( $\pm$ 0.011)	3.130( $\pm$ 0.383)	2	1.73e-04( $\pm$ 1.64e-04)	0.758( $\pm$ 0.006)
honkamj	0.762( $\pm$ 0.012)	3.119( $\pm$ 0.365)	3	1.72e-03( $\pm$ 2.73e-04)	0.749( $\pm$ 0.006)
LoRA-FT	0.741( $\pm$ 0.016)	3.441( $\pm$ 0.423)	10	5.95e-04( $\pm$ 3.25e-04)	0.724( $\pm$ 0.009)
MadeForLife	0.737( $\pm$ 0.012)	3.188( $\pm$ 0.390)	4	4.06e-03( $\pm$ 2.09e-03)	0.733( $\pm$ 0.007)
lukasf	0.763( $\pm$ 0.012)	3.246( $\pm$ 0.396)	5	5.43e-03( $\pm$ 1.22e-02)	0.750( $\pm$ 0.007)
LYUI	0.763( $\pm$ 0.013)	3.197( $\pm$ 0.382)	6	5.03e-03( $\pm$ 4.45e-04)	0.749( $\pm$ 0.008)
TimH	0.719( $\pm$ 0.014)	3.530( $\pm$ 0.393)	12	0.00e+00( $\pm$ 0.00e+00)	0.704( $\pm$ 0.008)
VROC	0.706( $\pm$ 0.010)	3.781( $\pm$ 0.369)	20	9.87e-02( $\pm$ 3.20e-02)	0.695( $\pm$ 0.006)
DutchMasters	0.760( $\pm$ 0.012)	3.165( $\pm$ 0.383)	7	1.64e-03( $\pm$ 1.02e-03)	0.746( $\pm$ 0.008)
zhuoyuanw210	0.766( $\pm$ 0.012)	3.125( $\pm$ 0.371)	8	1.30e-03( $\pm$ 4.02e-04)	0.752( $\pm$ 0.007)
ANTSyN	0.745( $\pm$ 0.013)	3.282( $\pm$ 0.393)	12	0.00e+00( $\pm$ 0.00e+00)	0.730( $\pm$ 0.007)
DeedsBCV	0.698( $\pm$ 0.016)	3.673( $\pm$ 0.386)	21	1.95e-04( $\pm$ 4.33e-04)	0.680( $\pm$ 0.008)
FireANTsGreedy	0.749( $\pm$ 0.015)	3.398( $\pm$ 0.429)	11	0.00e+00( $\pm$ 0.00e+00)	0.732( $\pm$ 0.009)
FireANTsSyN	0.741( $\pm$ 0.014)	3.474( $\pm$ 0.428)	10	2.74e-05( $\pm$ 2.05e-05)	0.725( $\pm$ 0.009)
SynthMorph	0.720( $\pm$ 0.019)	3.442( $\pm$ 0.404)	17	6.38e-06( $\pm$ 6.73e-06)	0.699( $\pm$ 0.008)
TransMorph	0.752( $\pm$ 0.012)	3.244( $\pm$ 0.390)	11	1.08e-01( $\pm$ 2.28e-02)	0.748( $\pm$ 0.007)
uniGradCON	0.740( $\pm$ 0.013)	3.378( $\pm$ 0.392)	11	1.51e-05( $\pm$ 2.35e-05)	0.728( $\pm$ 0.008)
uniGradCONiso	0.754( $\pm$ 0.012)	3.230( $\pm$ 0.385)	11	3.38e-05( $\pm$ 7.31e-05)	0.740( $\pm$ 0.008)
VEA	0.763( $\pm$ 0.014)	3.075( $\pm$ 0.375)	4	8.12e-03( $\pm$ 1.71e-03)	0.748( $\pm$ 0.006)
VoxelMorph	0.720( $\pm$ 0.020)	3.773( $\pm$ 0.482)	19	4.86e-01( $\pm$ 7.56e-02)	0.698( $\pm$ 0.012)
ZeroDisplacement	0.569( $\pm$ 0.031)	4.590( $\pm$ 0.518)	22	0.00e+00( $\pm$ 0.00e+00)	0.534( $\pm$ 0.015)

TABLE A6  
ADNI 1.5T Subject to Atlas.

Method	DSC	HD95	Ranking	NDV	DSC30
	Mean( $\pm$ Std. Dev.)	Mean( $\pm$ Std. Dev.)	(ACC)	Mean( $\pm$ Std. Dev.)	Mean( $\pm$ Std. Dev.)
Bailling	0.799( $\pm$ 0.012)	2.660( $\pm$ 0.236)	3	1.72e-02( $\pm$ 9.82e-03)	0.785( $\pm$ 0.007)
next-gen-nn	0.787( $\pm$ 0.018)	2.704( $\pm$ 0.285)	8	2.20e-04( $\pm$ 2.09e-04)	0.765( $\pm$ 0.011)
honkamj	0.791( $\pm$ 0.015)	2.636( $\pm$ 0.255)	4	2.31e-03( $\pm$ 5.43e-04)	0.773( $\pm$ 0.009)
LoRA-FT	0.764( $\pm$ 0.020)	2.964( $\pm$ 0.384)	10	3.42e-03( $\pm$ 3.42e-03)	0.739( $\pm$ 0.015)
MadeForLife	0.797( $\pm$ 0.014)	2.662( $\pm$ 0.258)	2	7.56e-03( $\pm$ 3.31e-03)	0.780( $\pm$ 0.009)
lukasf	0.785( $\pm$ 0.014)	2.774( $\pm$ 0.276)	10	8.75e-02( $\pm$ 2.04e-02)	0.768( $\pm$ 0.009)
LYUI	0.784( $\pm$ 0.018)	2.747( $\pm$ 0.289)	10	6.95e-03( $\pm$ 1.18e-03)	0.762( $\pm$ 0.011)
TimH	0.735( $\pm$ 0.019)	2.995( $\pm$ 0.261)	17	0.00e+00( $\pm$ 0.00e+00)	0.712( $\pm$ 0.012)
VROC	0.647( $\pm$ 0.032)	3.677( $\pm$ 0.335)	21	8.03e-02( $\pm$ 3.54e-02)	0.611( $\pm$ 0.016)
DutchMasters	0.793( $\pm$ 0.012)	2.603( $\pm$ 0.248)	1	6.03e-03( $\pm$ 2.76e-03)	0.779( $\pm$ 0.007)
zhuoyuanw210	0.789( $\pm$ 0.017)	2.739( $\pm$ 0.299)	7	3.52e-03( $\pm$ 1.63e-03)	0.769( $\pm$ 0.011)
ANTSyN	0.759( $\pm$ 0.020)	2.806( $\pm$ 0.268)	17	0.00e+00( $\pm$ 0.00e+00)	0.736( $\pm$ 0.015)
DeedsBCV	0.700( $\pm$ 0.021)	3.230( $\pm$ 0.281)	20	2.25e-04( $\pm$ 6.74e-04)	0.674( $\pm$ 0.012)
FireANTsGreedy	0.767( $\pm$ 0.022)	2.928( $\pm$ 0.300)	11	0.00e+00( $\pm$ 0.00e+00)	0.741( $\pm$ 0.015)
FireANTsSyN	0.755( $\pm$ 0.023)	3.062( $\pm$ 0.382)	10	5.05e-05( $\pm$ 3.32e-05)	0.726( $\pm$ 0.014)
SynthMorph	0.718( $\pm$ 0.023)	3.023( $\pm$ 0.318)	16	6.53e-06( $\pm$ 1.47e-05)	0.690( $\pm$ 0.014)
TransMorph	0.790( $\pm$ 0.014)	2.737( $\pm$ 0.285)	8	1.47e-01( $\pm$ 3.32e-02)	0.773( $\pm$ 0.010)
uniGradCON	0.765( $\pm$ 0.018)	2.892( $\pm$ 0.331)	11	6.94e-05( $\pm$ 8.80e-05)	0.743( $\pm$ 0.011)
uniGradCONiso	0.790( $\pm$ 0.013)	2.599( $\pm$ 0.258)	4	5.32e-04( $\pm$ 5.03e-04)	0.774( $\pm$ 0.008)
VEA	0.783( $\pm$ 0.016)	2.658( $\pm$ 0.254)	9	1.25e-02( $\pm$ 2.79e-03)	0.763( $\pm$ 0.010)
VoxelMorph	0.739( $\pm$ 0.028)	3.356( $\pm$ 0.473)	19	6.83e-01( $\pm$ 1.67e-01)	0.706( $\pm$ 0.021)
ZeroDisplacement	0.542( $\pm$ 0.034)	4.364( $\pm$ 0.495)	22	0.00e+00( $\pm$ 0.00e+00)	0.502( $\pm$ 0.021)

## ADNI 1.5T

## ADNI 3T

TABLE A4  
ADNI 1.5T Inter-subject.

Method	DSC	HD95	Ranking	NDV	DSC30
	Mean( $\pm$ Std. Dev.)	Mean( $\pm$ Std. Dev.)	(ACC)	Mean( $\pm$ Std. Dev.)	Mean( $\pm$ Std. Dev.)
Bailling	0.763( $\pm$ 0.011)	3.051( $\pm$ 0.240)	7	5.08e-02( $\pm$ 1.19e-02)	0.750( $\pm$ 0.008)
next-gen-nn	0.769( $\pm$ 0.013)	2.986( $\pm$ 0.255)	3	4.09e-04( $\pm$ 2.90e-04)	0.754( $\pm$ 0.009)
honkamj	0.774( $\pm$ 0.011)	2.790( $\pm$ 0.227)	1	3.24e-03( $\pm$ 6.01e-04)	0.761( $\pm$ 0.008)
LoRA-FT	0.731( $\pm$ 0.018)	3.507( $\pm$ 0.390)	13	3.86e-03( $\pm$ 2.27e-03)	0.710( $\pm$ 0.014)
MadeForLife	0.772( $\pm$ 0.012)	2.985( $\pm$ 0.271)	2	1.81e-02( $\pm$ 3.97e-03)	0.757( $\pm$ 0.009)
lukasf	0.758( $\pm$ 0.013)	3.132( $\pm$ 0.272)	6	2.52e-01( $\pm$ 4.72e-02)	0.743( $\pm$ 0.008)
LYUI	0.766( $\pm$ 0.013)	3.032( $\pm$ 0.286)	4	1.38e-02( $\pm$ 1.70e-03)	0.750( $\pm$ 0.009)
TimH	0.721( $\pm$ 0.013)	3.326( $\pm$ 0.253)	10	0.00e+00( $\pm$ 0.00e+00)	0.705( $\pm$ 0.008)
VROC	0.753( $\pm$ 0.015)	3.386( $\pm$ 0.329)	11	8.95e-02( $\pm$ 3.37e-02)	0.735( $\pm$ 0.010)
DutchMasters	0.768( $\pm$ 0.012)	2.947( $\pm$ 0.249)	4	4.20e-03( $\pm$ 1.62e-03)	0.754( $\pm$ 0.008)
zhuoyuanw210	0.760( $\pm$ 0.013)	3.036( $\pm$ 0.273)	5	8.84e-03( $\pm$ 1.84e-03)	0.745( $\pm$ 0.009)
ANTSyN	0.731( $\pm$ 0.020)	3.224( $\pm$ 0.281)	11	0.00e+00( $\pm$ 0.00e+00)	0.709( $\pm$ 0.022)
DeedsBCV	0.680( $\pm$ 0.014)	3.744( $\pm$ 0.272)	21	5.02e-04( $\pm$ 1.54e-03)	0.664( $\pm$ 0.008)
FireANTsGreedy	0.741( $\pm$ 0.015)	3.436( $\pm$ 0.359)	10	0.00e+00( $\pm$ 0.00e+00)	0.722( $\pm$ 0.011)
FireANTsSyN	0.738( $\pm$ 0.017)	3.497( $\pm$ 0.382)	10	2.98e-05( $\pm$ 2.18e-05)	0.718( $\pm$ 0.012)
SynthMorph	0.697( $\pm$ 0.017)	3.488( $\pm$ 0.326)	18	3.35e-06( $\pm$ 1.21e-05)	0.677( $\pm$ 0.012)
TransMorph	0.757( $\pm$ 0.013)	3.171( $\pm$ 0.288)	11	3.47e-01( $\pm$ 6.08e-02)	0.741( $\pm$ 0.009)
uniGradCON	0.741( $\pm$ 0.015)	3.318( $\pm$ 0.338)	12	2.31e-04( $\pm$ 1.71e-04)	0.723( $\pm$ 0.011)
uniGradCONiso	0.738( $\pm$ 0.013)	3.088( $\pm$ 0.284)	10	3.55e-04( $\pm$ 2.90e-04)	0.742( $\pm$ 0.009)
VEA	0.764( $\pm$ 0.012)	2.892( $\pm$ 0.238)	3	4.77e-02( $\pm$ 9.86e-03)	0.749( $\pm$ 0.008)
VoxelMorph	0.704( $\pm$ 0.024)	3.914( $\pm$ 0.463)	19	1.27e+00( $\pm$ 1.80e-01)	0.675( $\pm$ 0.019)
ZeroDisplacement	0.520( $\pm$ 0.030)	4.936( $\pm$ 0.475)	22	0.00e+00( $\pm$ 0.00e+00)	0.484( $\pm$ 0.020)

TABLE A7  
ADNI 3T Inter-subject.

Method	DSC	HD95	Ranking	NDV	DSC30
	Mean( $\pm$ Std. Dev.)	Mean( $\pm$ Std. Dev.)	(ACC)	Mean( $\pm$ Std. Dev.)	Mean( $\pm$ Std. Dev.)
Bailling	0.766( $\pm$ 0.014)	3.109( $\pm$ 0.325)	7	5.64e-02( $\pm$ 1.61e-02)	0.750( $\pm$ 0.012)
next-gen-nn	0.772( $\pm$ 0.015)	3.051( $\pm$ 0.310)	3	4.25e-04( $\pm$ 2.97e-04)	0.754( $\pm$ 0.012)
honkamj	0.777( $\pm$ 0.012)	2.821( $\pm$ 0.258)	1	3.16e-03( $\pm$ 6.65e-04)	0.762( $\pm$ 0.010)
LoRA-FT	0.732( $\pm$ 0.022)	3.601( $\pm$ 0.523)	13	3.24e-03( $\pm$ 2.02e-03)	0.706( $\pm$ 0.022)
MadeForLife	0.774( $\pm$ 0.015)	3.052( $\pm$ 0.400)	2	2.03e-02( $\pm$ 4.82e-03)	0.756( $\pm$ 0.015)
lukasf	0.761( $\pm$ 0.017)	3.201( $\pm$ 0.379)	9	2.72e-01( $\pm$ 5.40e-02)	0.742( $\pm$ 0.017)
LYUI	0.769( $\pm$ 0.017)	3.087( $\pm$ 0.406)	5	1.48e-02( $\pm$ 1.93e-03)	0.749( $\pm$ 0.017)
TimH	0.724( $\pm$ 0.016)	3.387( $\pm$ 0.357)	10	0.00e+00( $\pm$ 0.00e+00)	0.705( $\pm$ 0.012)
VROC	0.756( $\pm$ 0.019)	3.467( $\pm$ 0.461)	11	8.71e-02( $\pm$ 4.46e-02)	0.733( $\pm$ 0.015)
DutchMasters	0.768( $\pm$ 0.013)	3.046( $\pm$ 0.293)	4	4.81e-03( $\pm$ 2.07e-03)	0.752( $\pm$ 0.008)
zhuoyuanw210	0.762( $\pm$ 0.015)	3.112( $\pm$ 0.342)	6	9.34e-03( $\pm$ 1.89e-03)	0.743( $\pm$ 0.012)
ANTSyN	0.739( $\pm$ 0.015)	3.264( $\pm$ 0.356)	11	0.00e+00( $\pm$ 0.00e+00)	0.721( $\pm$ 0.010)
DeedsBCV	0.685( $\pm$ 0.017)	3.808( $\pm$ 0.343)	21	2.73e-04( $\pm$ 3.92e-04)	0.663( $\pm$ 0.012)
FireANTsGreedy	0.742( $\pm$ 0.020)	3.525( $\pm$ 0.489)	10	0.00e+00( $\pm$ 0.00e+00)	0.719( $\pm$ 0.019)
FireANTsSyN	0.740( $\pm$ 0.022)	3.587( $\pm$ 0.517)	10	3.48e-05( $\pm$ 2.21e-05)	0.714( $\pm$ 0.020)
SynthMorph	0.700( $\pm$ 0.022)	3.558( $\pm$ 0.446)	16	5.23e-06( $\pm$ 8.97e-06)	0.674( $\pm$ 0.018)
TransMorph	0.758( $\pm$ 0.019)	3.250( $\pm$ 0.417)	11	3.63e-01( $\pm$ 6.56e-02)	0.737( $\pm$ 0.019)
uniGradCON	0.742( $\pm$ 0.019)	3.391( $\pm$ 0.450)	12	2.46e-04( $\pm$ 2.03e-04)	0.720( $\pm$ 0.016)
uniGradCONiso	0.753( $\pm$ 0.017)	3.249( $\pm$ 0.426)	11	3.24e-04( $\pm$ 1.71e-04)	0.733( $\pm$ 0.015)
VEA	0.768( $\pm$ 0.014)	2.946( $\pm$ 0.304)	4	5.84e-02( $\pm$ 1.28e-02)	0.751( $\pm$ 0.011)
VoxelMorph	0.703( $\pm$ 0.028)	4.048( $\pm$ 0.589)	19	1.35e+00( $\pm$ 2.04e-01)	0.670( $\pm$ 0.026)
ZeroDisplacement	0.522( $\pm$ 0.031)	5.073( $\pm$ 0.617)	22	0.00e+00( $\pm$ 0.00e+00)	0.487( $\pm$ 0.024)

TABLE A5  
ADNI 1.5T Atlas to Subject.

Method	DSC	HD95	Ranking	NDV	DSC30
	Mean( $\pm$ Std. Dev.)	Mean( $\pm$ Std. Dev.)	(ACC)	Mean( $\pm$ Std. Dev.)	Mean( $\pm$ Std. Dev.)
Bailling	0.762( $\pm$ 0.016)	2.766( $\pm$ 0.257)	3	4.66e-02( $\pm$ 1.08e-02)	0.742( $\pm$ 0.010)
next-gen-nn	0.743( $\pm$ 0.025)	2.878( $\pm$ 0.333)	11	1.21e-04( $\pm$ 1.40e-04)	0.713( $\pm$ 0.015)
honkamj	0.765( $\pm$ 0.020)	2.594( $\pm$ 0.284)	2	9.02e-04( $\pm$ 2.38e-04)	0.741( $\pm$ 0.013)
LoRA-FT	0.744( $\pm$ 0.023)	3.007( $\pm$ 0.432)	17	9.80e-03( $\pm$ 5.15e-03)	0.716( $\pm$ 0.016)
MadeForLife	0.756( $\pm$ 0.020)	2.740( $\pm$ 0.291)	4	4.04e-03( $\pm$ 1.64e-03)	0.731( $\pm$ 0.012)
lukasf	0.763( $\pm$ 0.016)	2.798( $\pm$ 0.272)	6	3.07e-01( $\pm$ 6.54e-02)	0.744( $\pm$ 0.010)
LYUI	0.740( $\pm$ 0.022)	2.792( $\pm$ 0.313)	5	1.07e-02( $\pm$ 1.20e-03)	0.713( $\pm$ 0.014)
TimH	0.731( $\pm$ 0.019)	2.995( $\pm$ 0.286)	10	0.00e+00( $\pm$ 0.00e+00)	0.707( $\pm$ 0.013)
VROC	0.649( $\pm$ 0.036)	3.621( $\pm$ 0.372)	21	9.74e-02( $\pm$ 3.71e-02)	0.606( $\pm$ 0.019)
D					

TABLE A9  
ADNI 3T Subject to Atlas.

Method	DSC		Ranking (ACC)	NDV		DSC30
	Mean(±Std. Dev.)	Mean(±Std. Dev.)		Mean(±Std. Dev.)	Mean(±Std. Dev.)	
Bailling	0.801(±0.011)	2.659(±0.233)	3	1.81e-02(±1.21e-02)	0.787(±0.007)	
next-gen-nn	0.790(±0.018)	2.668(±0.278)	2	2.30e-04(±2.10e-04)	0.768(±0.011)	
honkamj	0.791(±0.014)	2.636(±0.252)	5	2.27e-03(±5.46e-04)	0.774(±0.008)	
LoRA-FT	0.765(±0.020)	2.924(±0.392)	6	2.89e-03(±2.77e-03)	0.740(±0.019)	
MadeForLife	0.796(±0.015)	2.660(±0.256)	4	8.57e-03(±3.57e-03)	0.779(±0.008)	
lukasf	0.784(±0.014)	2.766(±0.265)	10	8.84e-02(±2.15e-02)	0.767(±0.010)	
LYUI	0.784(±0.018)	2.743(±0.291)	7	7.13e-03(±1.50e-03)	0.761(±0.012)	
TimH	0.737(±0.020)	3.007(±0.261)	12	0.00e+00(±0.00e+00)	0.711(±0.014)	
VROC	0.642(±0.030)	3.806(±0.328)	19	9.72e-02(±3.86e-02)	0.605(±0.017)	
DutchMasters	0.792(±0.012)	2.589(±0.248)	1	6.21e-03(±3.57e-03)	0.776(±0.008)	
zhuoyuanw210	0.791(±0.017)	2.730(±0.310)	8	3.65e-03(±2.11e-03)	0.769(±0.011)	
ANTSySvN	0.762(±0.024)	2.801(±0.282)	11	1.29e-05(±1.22e-04)	0.735(±0.027)	
DeedsBCV	0.701(±0.022)	3.245(±0.286)	20	1.48e-04(±2.63e-04)	0.674(±0.015)	
FireANTsGreedy	0.769(±0.022)	2.922(±0.360)	10	0.00e+00(±0.00e+00)	0.741(±0.017)	
FireANTsSyN	0.759(±0.023)	3.011(±0.392)	10	4.62e-05(±3.51e-05)	0.729(±0.016)	
SynthMorph	0.717(±0.025)	3.030(±0.320)	16	6.07e-06(±1.16e-05)	0.686(±0.019)	
TransMorph	0.791(±0.014)	2.722(±0.269)	4	1.52e-01(±3.49e-02)	0.774(±0.010)	
uniGradICON	0.767(±0.017)	2.856(±0.333)	13	8.20e-03(±1.04e-04)	0.745(±0.013)	
uniGradICONiso	0.784(±0.013)	2.633(±0.255)	4	2.81e-04(±5.26e-04)	0.768(±0.009)	
VFA	0.784(±0.016)	2.646(±0.246)	7	1.25e-02(±2.88e-03)	0.764(±0.008)	
VoxelMorph	0.740(±0.029)	3.367(±0.503)	19	6.69e-01(±1.77e-01)	0.703(±0.025)	
ZeroDisplacement	0.546(±0.036)	4.376(±0.539)	25	0.00e+00(±0.00e+00)	0.502(±0.027)	

TABLE A12  
NIMH T1w Inter-subject.

Method	DSC		Ranking (ACC)	NDV		DSC30
	Mean(±Std. Dev.)	Mean(±Std. Dev.)		Mean(±Std. Dev.)	Mean(±Std. Dev.)	
Bailling	0.777(±0.012)	2.966(±0.261)	7	3.93e-02(±1.08e-02)	0.763(±0.008)	
next-gen-nn	0.779(±0.012)	2.927(±0.263)	8	2.75e-04(±1.53e-04)	0.765(±0.009)	
honkamj	0.783(±0.012)	2.713(±0.239)	1	2.91e-03(±4.82e-04)	0.769(±0.008)	
LoRA-FT	0.743(±0.018)	3.417(±0.398)	17	2.31e-03(±1.69e-03)	0.722(±0.015)	
MadeForLife	0.781(±0.015)	2.935(±0.301)	6	1.34e-02(±2.68e-03)	0.766(±0.010)	
lukasf	0.767(±0.014)	3.010(±0.298)	9	2.53e-01(±4.32e-02)	0.750(±0.010)	
LYUI	0.777(±0.013)	2.953(±0.292)	5	1.39e-02(±1.31e-03)	0.761(±0.009)	
TimH	0.731(±0.015)	3.272(±0.267)	16	0.00e+00(±0.00e+00)	0.716(±0.008)	
VROC	0.764(±0.014)	3.290(±0.327)	12	5.53e-02(±2.66e-02)	0.748(±0.010)	
DutchMasters	0.776(±0.012)	2.901(±0.246)	6	3.33e-03(±1.21e-03)	0.762(±0.008)	
zhuoyuanw210	0.773(±0.013)	2.940(±0.266)	8	6.09e-03(±1.02e-03)	0.758(±0.010)	
ANTSySvN	0.744(±0.014)	3.185(±0.290)	13	0.00e+00(±0.00e+00)	0.728(±0.009)	
DeedsBCV	0.692(±0.014)	3.722(±0.305)	18	5.15e-04(±3.66e-03)	0.676(±0.009)	
FireANTsGreedy	0.752(±0.016)	3.379(±0.384)	10	0.00e+00(±0.00e+00)	0.733(±0.013)	
FireANTsSyN	0.748(±0.017)	3.437(±0.400)	10	2.23e-05(±1.43e-05)	0.728(±0.014)	
SynthMorph	0.716(±0.017)	3.367(±0.333)	19	8.27e-06(±1.45e-05)	0.697(±0.013)	
TransMorph	0.766(±0.014)	3.123(±0.310)	10	3.43e-01(±5.30e-02)	0.748(±0.010)	
uniGradICON	0.750(±0.015)	3.250(±0.336)	11	1.24e-04(±9.74e-05)	0.733(±0.011)	
uniGradICONiso	0.763(±0.014)	3.085(±0.310)	11	1.93e-04(±1.73e-04)	0.747(±0.010)	
VFA	0.777(±0.012)	2.827(±0.247)	2	6.12e-02(±1.36e-02)	0.763(±0.008)	
VoxelMorph	0.723(±0.022)	3.736(±0.453)	20	1.21e+00(±1.61e-01)	0.697(±0.019)	
ZeroDisplacement	0.553(±0.030)	4.639(±0.451)	25	0.00e+00(±0.00e+00)	0.518(±0.020)	

NIMH - T1w

TABLE A13  
NIMH T2\*w Inter-subject.

Method	DSC		Ranking (ACC)	NDV		DSC30
	Mean(±Std. Dev.)	Mean(±Std. Dev.)		Mean(±Std. Dev.)	Mean(±Std. Dev.)	
Bailling	0.647(±0.034)	4.037(±0.461)	1	9.97e-03(±2.96e-03)	0.612(±0.042)	
next-gen-nn	0.649(±0.034)	4.034(±0.468)	1	1.55e-04(±6.18e-04)	0.614(±0.039)	
honkamj	0.651(±0.032)	3.873(±0.438)	7	1.99e-03(±4.62e-04)	0.618(±0.037)	
LoRA-FT	0.638(±0.031)	4.027(±0.457)	17	5.38e-03(±4.79e-03)	0.604(±0.033)	
MadeForLife	0.664(±0.032)	3.763(±0.411)	2	2.33e-02(±1.70e-03)	0.632(±0.039)	
lukasf	0.656(±0.032)	3.803(±0.394)	4	7.63e-02(±1.79e-02)	0.625(±0.039)	
LYUI	0.653(±0.031)	3.909(±0.430)	6	6.44e-01(±9.37e-04)	0.619(±0.035)	
TimH	0.640(±0.030)	3.999(±0.423)	15	0.00e+00(±0.00e+00)	0.609(±0.036)	
VROC	0.634(±0.037)	4.255(±0.529)	19	8.95e-02(±5.17e-02)	0.597(±0.046)	
DutchMasters	0.640(±0.035)	3.993(±0.489)	12	8.49e-04(±3.32e-03)	0.605(±0.044)	
zhuoyuanw210	0.642(±0.034)	4.044(±0.507)	11	1.51e-03(±8.24e-04)	0.606(±0.038)	
ANTSySvN	0.656(±0.035)	3.779(±0.447)	8	0.00e+00(±0.00e+00)	0.622(±0.045)	
DeedsBCV	0.625(±0.033)	4.247(±0.477)	14	2.51e-04(±8.15e-04)	0.594(±0.043)	
FireANTsGreedy	0.649(±0.034)	4.024(±0.444)	4	0.00e+00(±0.00e+00)	0.615(±0.041)	
FireANTsSyN	0.644(±0.031)	4.062(±0.433)	10	3.20e-05(±2.14e-05)	0.611(±0.035)	
SynthMorph	0.656(±0.028)	3.703(±0.379)	1	5.42e-07(±3.19e-06)	0.626(±0.033)	
TransMorph	0.653(±0.032)	3.858(±0.413)	5	1.48e-01(±3.22e-02)	0.620(±0.039)	
uniGradICON	0.628(±0.035)	4.127(±0.520)	18	1.09e-04(±3.73e-04)	0.592(±0.039)	
uniGradICONiso	0.639(±0.035)	3.987(±0.491)	15	2.61e-04(±2.44e-03)	0.605(±0.043)	
VFA	0.642(±0.030)	3.998(±0.421)	10	1.30e-02(±2.65e-03)	0.609(±0.039)	
VoxelMorph	0.627(±0.028)	4.174(±0.448)	14	5.74e-01(±1.08e-01)	0.594(±0.024)	
ZeroDisplacement	0.552(±0.030)	4.639(±0.453)	25	0.00e+00(±0.00e+00)	0.517(±0.020)	

TABLE A10  
NIMH T1w Atlas to Subject.

Method	DSC		Ranking (ACC)	NDV		DSC30
	Mean(±Std. Dev.)	Mean(±Std. Dev.)		Mean(±Std. Dev.)	Mean(±Std. Dev.)	
Bailling	0.791(±0.011)	2.581(±0.233)	7	3.30e-02(±8.07e-03)	0.776(±0.008)	
next-gen-nn	0.791(±0.015)	2.591(±0.237)	6	1.31e-04(±1.61e-04)	0.775(±0.010)	
honkamj	0.801(±0.012)	2.365(±0.237)	3	8.11e-04(±2.08e-04)	0.786(±0.008)	
LoRA-FT	0.772(±0.011)	2.668(±0.281)	15	7.45e-03(±3.60e-03)	0.759(±0.009)	
MadeForLife	0.796(±0.013)	2.513(±0.247)	5	3.56e-03(±1.27e-03)	0.779(±0.009)	
lukasf	0.785(±0.013)	2.671(±0.249)	11	2.74e-01(±5.20e-02)	0.769(±0.009)	
LYUI	0.786(±0.014)	2.565(±0.233)	9	1.26e-02(±1.57e-03)	0.767(±0.009)	
TimH	0.758(±0.020)	2.833(±0.219)	17	0.00e+00(±0.00e+00)	0.745(±0.007)	
VROC	0.726(±0.010)	3.228(±0.280)	20	8.10e-02(±2.93e-02)	0.701(±0.015)	
DutchMasters	0.795(±0.008)	2.450(±0.208)	2	1.53e-03(±6.56e-04)	0.786(±0.006)	
zhuoyuanw210	0.793(±0.009)	2.463(±0.221)	4	2.98e-03(±5.19e-04)	0.781(±0.007)	
ANTSySvN	0.781(±0.011)	2.600(±0.229)	10	0.00e+00(±0.00e+00)	0.768(±0.007)	
DeedsBCV	0.725(±0.012)	3.111(±0.257)	19	6.18e-04(±4.08e-03)	0.709(±0.008)	
FireANTsGreedy	0.784(±0.014)	2.765(±0.302)	10	0.00e+00(±0.00e+00)	0.767(±0.010)	
FireANTsSyN	0.783(±0.014)	2.703(±0.295)	15	1.69e-05(±1.70e-05)	0.766(±0.010)	
SynthMorph	0.749(±0.013)	2.747(±0.259)	16	6.95e-06(±9.22e-06)	0.734(±0.009)	
TransMorph	0.782(±0.014)	2.735(±0.264)	10	3.56e-01(±6.45e-02)	0.764(±0.009)	
uniGradICON	0.776(±0.009)	2.590(±0.238)	12	7.77e-05(±7.64e-05)	0.764(±0.007)	
uniGradICONiso	0.790(±0.008)	2.503(±0.208)	3	1.75e-04(±2.59e-04)	0.780(±0.006)	
VFA	0.787(±0.013)	2.515(±0.237)	6	5.13e-02(±1.32e-02)	0.770(±0.009)	
VoxelMorph	0.735(±0.017)	2.987(±0.332)	17	1.15e+00(±1.50e-01)	0.735(±0.012)	
ZeroDisplacement	0.596(±0.022)	3.835(±0.307)	25	0.00e+00(±0.00e+00)	0.570(±0.015)	

TABLE A11  
NIMH T1w Subject to Atlas.

Method	DSC		Ranking (ACC)	NDV		DSC30
	Mean(±Std. Dev.)	Mean(±Std. Dev.)		Mean(±Std. Dev.)	Mean(±Std. Dev.)	
Bailling	0.813(±0.008)	2.487(±0.189)	3	8.25e-03(±2.47e-03)	0.803(±0.006)	
next-gen-nn	0.811(±0.009)	2.448(±0.189)	1	1.80e-04(±1.59e-04)	0.800(±0.006)	
honkamj	0.806(±0.012)	2.424(±0.226)	2	2.05e-03(±4.09e-04)	0.791(±0.008)	
LoRA-FT	0.777(±0.011)	2.709(±0.282)	16	1.15e-03(±1.08e-03)	0.764(±0.009)	
MadeForLife	0.809(±0.011)	2.482(±0.219)	4	5.96e-03(±1.66e-03)	0.795(±0.008)	
lukasf	0.796(±0.008)	2.596(±0.208)	11	6.69e-02(±1.50e-02)	0.786(±0.006)	
LYUI	0.806(±0.012)	2.476(±0.221)	7	5.72e-03(±8.02e-04)	0.790(±0.009)	
TimH	0.760(±0.010)	2.844(±0.211)	17	0.00e+00(±0.00e+00)	0.747(±0.007)	
VROC	0.714(±0.020)	3.370(±0.256)	21	6.39e-02(±2.44e-02)	0.691(±0.015)	
DutchMasters	0.801(±0.008)	2.444(±0.204)	3	3.47e-03(±1.31e-03)	0.791(±0.006)	
zhuoyuanw210	0.809(±0.011)	2.440(±0.208)	5	2.06e-03(±5.49e-04)	0.795(±0.008)	
ANTSySvN	0.784(±0.015)	2.598(±0.224)	10	0.00e+00(±0.00e+00)	0.770(±0.019)	
DeedsBCV	0.729(±0.012)	3.059(±0.230)	20	2.18e-04(±6.37e-04)	0.715(±0.007)	
FireANTsGreedy	0.792(±0.013)	2.699(±0.271)	10	0.00e+00(±0.00e+00)	0.776(±0.009)	
FireANTsSyN	0.785(±0.015)	2.749(±0.305)	15	3.69e-05(±2.26e-05)	0.767(±0.011)	
SynthMorph	0.751(±0.015)	2.775(±0.255)	16	7.71e-06(±1.03e-05)	0.735(±0.009)	
TransMorph	0.803(±0.010)					

TABLE A15  
NIMH FLAIR Inter-subject.

Method	DSC	HD95	Ranking	NDV	DSC30
	Mean(±Std. Dev.)	Mean(±Std. Dev.)	(ACC)	Mean(±Std. Dev.)	Mean(±Std. Dev.)
Baillang	0.668(±0.039)	3.761(±0.545)	3	1.53e-02(±9.63e-03)	0.632(±0.045)
next-gen-nn	0.659(±0.047)	3.830(±0.751)	9	7.34e-05(±1.13e-04)	0.617(±0.061)
honkamj	0.662(±0.050)	3.722(±0.984)	2	2.22e-03(±7.96e-04)	0.620(±0.068)
LoRA-FT	0.646(±0.037)	3.926(±0.549)	7	3.85e-03(±3.56e-03)	0.610(±0.046)
MadeForLife	0.673(±0.033)	3.614(±0.392)	6	4.83e-03(±4.57e-03)	0.637(±0.029)
lukasf	0.663(±0.040)	3.744(±0.355)	4	1.10e-01(±4.28e-02)	0.626(±0.049)
LYU1	0.658(±0.034)	3.822(±0.409)	11	8.87e-03(±2.31e-03)	0.621(±0.035)
TimH	0.649(±0.039)	3.871(±0.534)	14	0.00e+00(±0.00e+00)	0.612(±0.049)
VROC	0.648(±0.054)	4.102(±1.518)	17	3.92e-02(±5.58e-02)	0.604(±0.076)
DutchMasters	0.655(±0.057)	3.897(±2.151)	7	2.02e-03(±2.01e-03)	0.614(±0.087)
zhuoyuanw210	0.656(±0.051)	3.858(±1.043)	10	2.78e-03(±1.33e-03)	0.613(±0.071)
ANTSyN	0.657(±0.057)	3.935(±1.986)	8	0.00e+00(±0.00e+00)	0.615(±0.088)
DeedsBCV	0.644(±0.059)	4.247(±2.562)	19	1.00e-03(±1.06e-02)	0.605(±0.093)
FireANTsGreedy	0.652(±0.047)	4.061(±0.875)	15	0.00e+00(±0.00e+00)	0.609(±0.061)
FireANTsSyN	0.647(±0.036)	4.034(±0.475)	16	1.65e-05(±1.16e-05)	0.609(±0.036)
SynthMorph	0.668(±0.023)	3.617(±0.350)	2	0.00e+00(±0.00e+00)	0.643(±0.022)
TransMorph	0.660(±0.040)	3.791(±0.528)	5	1.75e-01(±7.02e-02)	0.621(±0.049)
uniGradICON	0.641(±0.056)	4.118(±2.414)	13	1.33e-04(±2.06e-04)	0.599(±0.086)
uniGradICONiso	0.650(±0.057)	4.018(±2.336)	12	4.59e-04(±7.53e-04)	0.608(±0.086)
VFA	0.652(±0.035)	3.797(±0.434)	12	3.28e-02(±2.36e-02)	0.614(±0.033)
VoxelMorph	0.634(±0.034)	4.117(±0.499)	21	7.34e-01(±1.96e-01)	0.598(±0.040)
ZeroDisplacement	0.552(±0.030)	4.636(±0.453)	22	0.00e+00(±0.00e+00)	0.517(±0.020)

TABLE A18  
UltraCortex - 9.4T Subject to Atlas.

Method	DSC	HD95	Ranking	NDV	DSC30
	Mean(±Std. Dev.)	Mean(±Std. Dev.)	(ACC)	Mean(±Std. Dev.)	Mean(±Std. Dev.)
Baillang	0.783(±0.032)	2.911(±0.626)	7	1.23e-02(±4.29e-03)	0.747(±0.038)
next-gen-nn	0.784(±0.035)	2.844(±0.691)	2	2.65e-04(±1.91e-04)	0.745(±0.043)
honkamj	0.778(±0.031)	2.794(±0.616)	6	2.35e-03(±4.15e-04)	0.743(±0.038)
LoRA-FT	0.736(±0.031)	3.168(±0.697)	7	4.31e-03(±2.48e-03)	0.699(±0.033)
MadeForLife	0.787(±0.030)	2.832(±0.627)	7	7.03e-03(±1.82e-03)	0.753(±0.036)
lukasf	0.764(±0.034)	2.963(±0.624)	10	1.01e-01(±2.11e-02)	0.725(±0.039)
LYU1	0.781(±0.031)	2.846(±0.653)	5	8.19e-03(±1.08e-03)	0.746(±0.037)
TimH	0.735(±0.033)	3.182(±0.642)	17	0.00e+00(±0.00e+00)	0.696(±0.038)
VROC	0.694(±0.026)	3.633(±0.650)	21	9.02e-02(±7.41e-02)	0.663(±0.022)
DutchMasters	0.760(±0.028)	2.919(±0.688)	9	1.14e-02(±6.84e-03)	0.728(±0.031)
zhuoyuanw210	0.781(±0.031)	2.855(±0.668)	8	2.35e-03(±7.61e-04)	0.745(±0.037)
ANTSyN	0.756(±0.034)	2.949(±0.627)	11	0.00e+00(±0.00e+00)	0.716(±0.041)
DeedsBCV	0.696(±0.027)	3.415(±0.596)	20	9.95e-05(±1.84e-04)	0.663(±0.027)
FireANTsGreedy	0.762(±0.036)	3.092(±0.677)	10	0.00e+00(±0.00e+00)	0.720(±0.041)
FireANTsSyN	0.756(±0.034)	3.144(±0.703)	16	3.14e-05(±1.85e-05)	0.717(±0.039)
SynthMorph	0.711(±0.034)	3.213(±0.706)	10	7.31e-06(±1.05e-05)	0.670(±0.036)
TransMorph	0.776(±0.035)	2.912(±0.649)	11	1.61e-01(±2.71e-02)	0.735(±0.041)
uniGradICON	0.738(±0.031)	3.140(±0.743)	15	8.53e-05(±7.06e-05)	0.702(±0.034)
uniGradICONiso	0.756(±0.030)	2.977(±0.690)	12	4.57e-04(±7.50e-04)	0.721(±0.035)
VFA	0.782(±0.030)	2.763(±0.596)	5	1.22e-02(±2.15e-03)	0.750(±0.037)
VoxelMorph	0.733(±0.043)	3.496(±0.785)	18	6.33e-01(±2.13e-01)	0.681(±0.049)
ZeroDisplacement	0.568(±0.045)	4.272(±0.772)	22	0.00e+00(±0.00e+00)	0.513(±0.043)

## Macaque (Non-human Brain)

TABLE A19  
Macaque (Non-human Brain) Inter-subject.

Method	DSC	HD95	Ranking	NDV	DSC30
	Mean(±Std. Dev.)	Mean(±Std. Dev.)	(ACC)	Mean(±Std. Dev.)	Mean(±Std. Dev.)
Baillang	0.768(±0.072)	4.496(±3.238)	10	3.55e-03(±1.04e-02)	0.672(±0.031)
next-gen-nn	0.769(±0.076)	4.450(±3.269)	9	2.18e-06(±1.36e-05)	0.669(±0.032)
honkamj	0.773(±0.074)	4.349(±3.223)	3	3.78e-04(±2.48e-04)	0.674(±0.032)
LoRA-FT	0.738(±0.075)	4.552(±3.207)	11	1.76e-03(±2.73e-03)	0.660(±0.030)
MadeForLife	0.777(±0.075)	4.318(±3.233)	7	1.22e-03(±1.04e-03)	0.677(±0.031)
lukasf	0.772(±0.075)	4.362(±3.223)	8	4.99e-02(±2.86e-02)	0.672(±0.030)
LYU1	0.767(±0.074)	4.361(±3.128)	6	2.72e-02(±1.91e-03)	0.670(±0.034)
TimH	0.753(±0.076)	4.494(±3.180)	10	0.00e+00(±0.00e+00)	0.651(±0.031)
VFA	0.750(±0.072)	4.643(±3.035)	12	1.61e-02(±1.52e-02)	0.659(±0.030)
DutchMasters	0.765(±0.072)	4.430(±3.212)	11	1.34e-04(±2.77e-04)	0.670(±0.029)
zhuoyuanw210	0.760(±0.073)	4.497(±3.188)	13	3.70e-04(±1.93e-04)	0.662(±0.028)
ANTSyN	0.771(±0.077)	4.385(±3.252)	8	0.00e+00(±0.00e+00)	0.667(±0.032)
DeedsBCV	0.762(±0.077)	4.498(±3.259)	14	1.38e-05(±7.15e-05)	0.658(±0.030)
FireANTsGreedy	0.775(±0.075)	4.358(±3.225)	2	0.00e+00(±0.00e+00)	0.675(±0.033)
FireANTsSyN	0.766(±0.074)	4.427(±3.219)	10	7.45e-06(±1.06e-05)	0.670(±0.033)
SynthMorph	0.748(±0.077)	4.612(±3.231)	19	0.00e+00(±0.00e+00)	0.648(±0.030)
TransMorph	0.768(±0.075)	4.396(±3.206)	7	5.03e-02(±2.94e-02)	0.669(±0.030)
uniGradICON	0.757(±0.075)	4.497(±3.180)	16	2.67e-05(±7.97e-05)	0.659(±0.030)
uniGradICONiso	0.767(±0.076)	4.402(±3.223)	9	9.65e-05(±4.00e-04)	0.667(±0.030)
VFA	0.692(±0.072)	5.095(±2.963)	21	2.88e-01(±1.37e-01)	0.603(±0.027)
VoxelMorph	0.756(±0.075)	4.521(±3.139)	17	3.38e-01(±1.11e-01)	0.657(±0.028)
ZeroDisplacement	0.665(±0.074)	5.331(±3.105)	22	0.00e+00(±0.00e+00)	0.571(±0.029)

## ACKNOWLEDGMENTS

We thank Lin Tian and Rohit Jena for their helpful discussions and guidance in the implementation of several of the baseline methods. We also thank Jiafeng Zhu for valuable input on statistical analysis.

This work is supported by grants from the National Institutes of Health (NIH), United States, R01CA297470 (PI: Y. Du), R01EB031023 (PI: Y. Du), U01EB031798 (PI: G. Sgouros), P01CA272222 (PI: G. Sgouros), R01CA253923 (PI: F. Maldonado), and R01CA275015 (PI: M.E. Lenburg). Yihao Liu is supported by NIH grants 5R01HL169944-02, 1U24AG074855-01, and 1R01MH121620-01. The views expressed in written conference materials or publications and by speakers and moderators do not necessarily reflect the official policies of the NIH; nor does mention by trade names, commercial practices, or organizations imply endorsement by the U.S. Government.

## REFERENCES

- 1] K. Murphy, B. van Ginneken, J. M. Reinhardt, S. Kabus, K. Ding, X. Deng, K. Cao, K. Du, G. E. Christensen, V. Garcia, T. Vercauteren, N. Ayache, O. Commowick, G. Malandain, B. Glocker, N. Paragios, N. Navab, V. Gorunova, J. Sporning, M. de Bruijne, X. Han, M. P. Heinrich, J. A. Schnabel, M. Jenkinson, C. Lorenz, M. Modat, J. R. McClelland, S. Ourselin, S. E. A. Muenzing, M. A. Viergever, D. De Nigris, D. L. Collins, T. Arbel, M. Peroni, R. Li, G. C. Sharp, A. Schmidt-Richberg, J. Ehrhardt, R. Werner,

## UltraCortex - 9.4T

TABLE A16  
UltraCortex - 9.4T Inter-subject.

Method	DSC	HD95	Ranking	NDV	DSC30
	Mean(±Std. Dev.)	Mean(±Std. Dev.)	(ACC)	Mean(±Std. Dev.)	Mean(±Std. Dev.)
Baillang	0.736(±0.042)	3.576(±0.663)	7	4.50e-02(±1.09e-02)	0.678(±0.024)
next-gen-nn	0.741(±0.044)	3.516(±0.692)	6	4.17e-04(±3.30e-04)	0.680(±0.026)
honkamj	0.745(±0.040)	3.288(±0.649)	2	2.87e-03(±5.25e-04)	0.688(±0.024)
LoRA-FT	0.702(±0.046)	3.959(±0.732)	12	5.96e-03(±3.23e-03)	0.639(±0.027)
MadeForLife	0.746(±0.040)	3.479(±0.659)	2	1.70e-02(±5.09e-03)	0.691(±0.023)
lukasf	0.728(±0.043)	3.639(±0.653)	3	3.29e-01(±6.31e-02)	0.669(±0.025)
LYU1	0.739(±0.041)	3.510(±0.658)	8	2.23e-02(±3.37e-03)	0.682(±0.024)
TimH	0.696(±0.040)	3.823(±0.655)	16	0.00e+00(±0.00e+00)	0.641(±0.023)
VROC	0.721(±0.050)	3.919(±0.788)	12	5.24e-02(±2.44e-02)	0.651(±0.027)
DutchMasters	0.733(±0.044)	3.532(±0.660)	6	6.64e-03(±2.44e-03)	0.672(±0.025)
zhuoyuanw210	0.730(±0.041)	3.556(±0.655)	9	9.40e-03(±2.01e-03)	0.674(±0.026)
ANTSyN	0.702(±0.052)	3.783(±0.768)	14	0.00e+00(±0.00e+00)	0.636(±0.049)
DeedsBCV	0.657(±0.039)	4.218(±0.632)	19	1.89e-04(±4.80e-04)	0.605(±0.025)
FireANTsGreedy	0.712(±0.046)	3.931(±0.746)	10	0.00e+00(±0.00e+00)	0.649(±0.028)
FireANTsSyN	0.709(±0.046)	4.012(±0.766)	15	1.44e-05(±9.53e-06)	0.647(±0.029)
SynthMorph	0.670(±0.044)	3.966(±0.735)	15	5.71e-06(±1.01e-05)	0.612(±0.030)
TransMorph	0.729(±0.042)	3.658(±0.652)	10	4.44e-01(±7.67e-02)	0.671(±0.025)
uniGradICON	0.707(±0.048)	3.857(±0.747)	13	3.51e-04(±3.58e-04)	0.641(±0.027)
uniGradICONiso	0.720(±0.044)	3.734(±0.718)	11	5.50e-04(±5.93e-04)	0.658(±0.026)
VFA	0.741(±0.040)	3.371(±0.627)	3	1.89e-01(±6.25e-02)	0.686(±0.024)
VoxelMorph	0.677(±0.048)	4.294(±0.755)	19	1.82e+00(±3.27e-01)	0.612(±0.030)
ZeroDisplacement	0.520(±0.042)	5.172(±0.748)	22	0.00e+00(±0.00e+00)	0.468(±0.023)

TABLE A17  
UltraCortex - 9.4T Atlas to Subject.

Method	DSC	HD95	Ranking	NDV	DSC30
	Mean(±Std. Dev.)	Mean(±Std. Dev.)	(ACC)	Mean(±Std. Dev.)	Mean(±Std. Dev.)
Baillang	0.751(±0.027)	3.044(±0.574)	12	4.41e-02(±9.16e-03)	0.719(±0.027)
next-gen-nn	0.762(±0.033)	2.968(±0.625)	5	1.52e-04(±1.71e-04)	0.723(±0.039)
honkamj	0.767(±0.029)	2.767(±0.590)	7	7.54e-04(±2.12e-04)	0.734(±0.034)
LoRA-FT	0.720(±0.029)	3.191(±0.619)	10	2.82e-02(±1.25e-02)	0.686(±0.027)
MadeForLife	0.765(±0.029)	2.904(±0.606)	6	3.67e-03(±1.06e-03)	0.732(±0.034)
lukasf	0.753(±0.029)	2.993(±0.552)	2	4.08e-01(±8.22e-02)	0.719(±0.033)
LYU1	0.755(±0.028)	2.940(±0.586)	3	1.82e-02(±2.60e-03)	0.722(±0.031)
TimH	0.732(±0.031)	3.157(±0.571)	15	0.00e+00(±0.00e+00)	0.695(±0.035)
VROC	0.696(±0.026)	3.516(±0.554)	20	7.95e-02(±2.35e-02)	0.664(±0.019)
DutchMasters	0.736(±0.027)	3.013(±0.527)	11	7.30e-03(±5.66e-03)	0.703(±0.017)
zhuoyuanw210	0.735(±0.027)	2.860(±0.547)	8	5.56e-03(±1.12e-03)	0.722(±0.028)
ANTSyN	0.750(±0.033)	2.963(±0.583)	8	0.00e+00(±0.00e+00)	0.711(±0.038)
DeedsBCV	0.691(±0.025)	3.481(±0.544)	21	2.00e-04(±4.58e-04)	0.660(±0.024)
FireANTsGreedy	0.752(±0.035)	3.114(±0.686)	11	0.00e+00(±0.00e+00)	0.710(±0.041)
FireANTsSyN	0.747(±0.036)	3.201(±0.729)	19	1.47e-05(±1.09e-05)	0.705(±0.042)
SynthMorph	0.707(±0.033)	3.225(±0.640)	16	6.03e-06(±6.71e-06)	0.667(±0.033)
TransMorph	0.754(±0.031)	3.064(±0.570)	6	5.04e-01(±8.10e-02)	0.718(±0.035)
uniGradICON	0.726(±0.028)	3.118(±0.589)	10	1.03e-03(±1.51e-03)	0.693(±0.026)
uniGradICONiso	0.741(±0.027)	3.012(±0.549)	11	1.33e-03(±2.30e-03)	0.709(±0.026)
VFA	0.760(±0.028)	2.835(±0.585)	2	1.58e-01(±5.25e-02)	0.729(±0.034)
VoxelMorph	0.715(±0.039)	3.406(±0.708)	18	1.61e+00(±3.08e-01)	0.670(±0.044)
ZeroDisplacement	0.568(±0.045)	4.272(±0.772)	22	0.00e+00(±0.00e+00)	0.513(±0.043)

- D. Smeets, D. Loeckx, G. Song, N. Tustison, B. Avants, J. C. Gee, M. Staring, S. Klein, B. C. Stoel, M. Urschler, M. Werlberger, J. Vandemeulebroucke, S. Rit, D. Sarrut, and J. P. W. Pluim, "Evaluation of Registration Methods on Thoracic CT: The EMPIRE10 Challenge," *IEEE Trans. Med. Imag.*, vol. 30, no. 11, pp. 1901–1920, 2011.
- [2] K. Sirinukunwattana, J. P. W. Pluim, H. Chen, X. Qi, P.-A. Heng, Y. B. Guo, L. Y. Wang, B. J. Matuszewski, E. Bruni, U. Sanchez, A. Böhm, O. Ronneberger, B. B. Cheikh, D. Racoceanu, P. Kainz, M. Pfeiffer, M. Urschler, D. R. J. Snead, and N. M. Rajpoot, "Gland Segmentation in Colon Histology Images: The GlaS Challenge Contest," *Medical Image Analysis*, vol. 35, pp. 489–502, 2017.
- [3] L. Maier-Hein, M. Eisenmann, A. Reinke, S. Onogur, M. Stankovic, P. Scholz, T. Arbel, H. Bogunovic, A. P. Bradley, A. Carass, C. Feldmann, A. F. Frangi, P. M. Full, B. van Ginneken, A. Hanbury, K. Honauer, M. Kozubek, B. A. Landman, K. März, O. Maier, K. Maier-Hein, B. H. Menze, H. Müller, P. F. Neher, W. Niessen, N. Rajpoot, G. C. Sharp, K. Sirinukunwattana, S. Speidel, C. Stock, D. Stoyanov, A. Aziz Taha, F. van der Sommen, C.-W. Wang, M.-A. Weber, G. Zheng, P. Jannin, and A. Kopp-Schneider, "Is the winner really the best? A critical analysis of common research practice in biomedical image analysis competitions," *Nature Communications*, vol. 9, no. 1, p. 5217, 2018.
- [4] S. S. Halabi, L. M. Prevedello, J. Kalpathy-Cramer, A. B. Mamonov, A. Bilbily, M. Cicero, I. Pan, L. A. Pereira, R. T. Sousa, N. Abdala, F. C. Kitamura, H. H. Thodberg, L. Chen, G. Shih, K. Andriole, M. D. Kohli, B. J. Erickson, and A. E. Flanders, "The RSNA pediatric bone age machine learning challenge," *Radiology*, vol. 290, no. 2, pp. 498–503, 2019.
- [5] M. Antonelli, A. Reinke, S. Bakas, K. Farahani, A. Kopp-Schneider, B. A. Landman, G. Litjens, B. Menze, O. Ronneberger, R. M. Summers, B. van Ginneken11, M. Bilello, P. Bilic, P. F. Christ, R. K. G. Do, M. J. Gollub, S. H. Heckers, H. Huisman, W. R. Jarnagin, M. K. McHugo, S. Napel, J. S. G. Pernicka, K. Rhode1, C. Tobon-Gomez, E. Vorontsov, J. A. Meakin1, S. Ourselin, M. Wiesenfarth, P. Arbeláez, B. Bae, S. Chen, L. Daza, J. Feng, B. He, F. Isensee, Y. Ji, F. Jia, I. Kim, K. Maier-Hein, D. Merhof, A. Pai, B. Park, M. Perslev, R. Rezaifar, O. Rippel, I. Sarasua, W. Shen, J. Son, C. Wachinger, L. Wang, Y. Wang, Y. Xia, D. Xu, Z. Xu, Y. Zheng, A. L. Simpson, L. Maier-Hein, and M. J. Cardoso, "The Medical Segmentation Decathlon," *Nature Communications*, vol. 13, no. 1, p. 4128, 2022.
- [6] A. Hering, L. Hansen, T. C. W. Mok, A. C. S. Chung, H. Siebert, S. Häger, A. Lange, S. Kuckertz, S. Heldmann, W. Shao, S. Vesal, M. Rusu, G. Sonn, T. Estienne, M. Vakalopoulou, L. Han, Y. Huang, P.-T. Yap, M. Brudfors, Y. Balbastre, S. Joutard, M. Modat, G. Lifshitz, D. Raviv, J. Lv, Q. Li, V. Jaouen, D. Visvikis, C. Fourcade, M. Rubeaux, W. Pan, Z. Xu, B. Jian, F. De Benetti, M. Wodzinski, N. Gunnarsson, J. Sjölund, D. Grzech, H. Qiu, Z. Li, A. Thorley, J. Duan, C. Großbröhm, A. Hoopes, I. Reinertsen, Y. Xiao, B. Landman, Y. Huo, K. Murphy, N. Lessmann, B. van Ginneken, A. V. Dalca, and M. P. Heinrich, "Learn2Reg: Comprehensive multi-task medical image registration challenge, dataset and evaluation in the era of deep learning," *IEEE Trans. Med. Imag.*, vol. 42, no. 3, pp. 697–712, 2023.
- [7] B. H. Menze, A. Jakab, S. Bauer, J. Kalpathy-Cramer, K. Farahani, J. Kirby, Y. Burren, N. Porz, J. Slotboom, R. Wiest, L. Lanczi, E. Gerstner, M.-A. Weber, T. Arbel, B. B. Avants, N. Ayache, P. Buendia, D. L. Collins, N. Cordier, J. J. Corso, A. Criminisi, T. Das, H. Delingette, Ç. Demiralp, C. R. Durst, M. Dojat, S. Doyle, J. Festa, F. Forbes, E. Geremia, B. Glocker, P. Golland, X. Guo, A. Hamamci, K. M. Iftekharuddin, R. Jena, N. M. John, E. Konukoglu, D. Lashkari, J. A. Mariz, R. Meier, S. Pereira, D. Precup, S. J. Price, T. Riklin-Raviv, S. M. S. Reza, M. Ryan, D. Sarikaya, L. Schwartz, H.-C. Shin, J. Shotton, C. A. Silva, N. Sousa, N. K. Subbanna, G. Székely, T. J. Taylor, O. M. Thomas, N. J. Tustison, G. Unal, F. Vasseur, M. Wintermark, D. H. Ye, L. Zhao, B. Zhao, D. Zikic, M. Prastawa, M. Reyes, and K. Van Leemput, "The Multimodal Brain Tumor Image Segmentation Benchmark (BRATS)," *IEEE Trans. Med. Imag.*, vol. 34, no. 10, pp. 1993–2024, 2015.
- [8] O. Maier, B. H. Menze, J. von der Gablentz, L. Häni, M. P. Heinrich, M. Liebrand, S. Winzeck, A. Basit, P. Bentley, L. Chen, D. Christiaens, F. Dutil, K. Egger, C. Feng, B. Glocker, M. Götz, T. Haeck, H.-L. Halme, M. Havaei, K. M. Iftekharuddin, P.-M. Jodoin, K. Kamnitsas, E. Kellner, A. Korvenoja, H. Larochelle, C. Ledig, J.-H. Lee, F. Maes, Q. Mahmood, K. H. Maier-Hein, R. McKinley, J. Muschelli, C. Pal, L. Pei, J. R. Rangarajan, S. M. S. Reza, D. Robben, D. Rueckert, E. Salli, P. Suetens, C.-W. Wang, M. Wilms, J. S. Kirschke, U. M. Krämer, T. F. Munte, P. Schramm, R. Wiest, H. Handels, and M. Reyes, "ISLES 2015 - A public evaluation benchmark for ischemic stroke lesion segmentation from multispectral MRI," *Medical Image Analysis*, vol. 35, pp. 250–269, 2017.
- [9] A. Carass, S. Roy, A. Jog, J. L. Cuzzocreo, E. Magrath, A. Gherman, J. Button, J. Nguyen, F. Prados, C. H. Sudre, M. J. Cardoso, N. Cawley, O. Ciccarelli, C. A. M. Wheeler-Kingshott, S. Ourselin, L. Catanese, H. Deshpande, P. Maurel, O. Commowick, C. Barillot, X. Tomas-Fernandez, S. K. Warfield, S. Vaidya, A. Chunduru, R. Muthuganapathy, G. Krishnamurthi, A. Jesson, T. Arbel, O. Maier, H. Handels, L. O. Ithel, D. Unay, S. Jain, D. M. Sima, D. Smeets, M. Ghafoorian, B. Platel, A. Birenbaum, H. Greenspan, P.-L. Bazin, P. A. Calabresi, C. Crainiceanu, L. M. Ellingsen, D. S. Reich, J. L. Prince, and D. L. Pham, "Longitudinal multiple sclerosis lesion segmentation: Resource & challenge," *NeuroImage*, vol. 148, pp. 77–102, 2017.
- [10] O. Commowick, A. Istace, M. Kain, B. Laurent, F. Leray, M. Simon, S. C. Pop, P. Girard, R. Ameli, J. C. Ferré, A. Kerbrat, T. Tourdias, F. Cervenansky, T. Glatard, J. Beaumont, S. Doyle, F. Forbes, J. Knight, A. Khademi, A. Mahbod, C. Wang, R. McKinley, F. Wagner, J. Muschelli, E. Sweeney, E. Roura, X. Lladó, M. M. Santos, W. P. Santos, A. G. Silva-Filho, X. Tomas-Fernandez, H. Urien, I. Bloch, S. Valverde, M. Cabezas, F. J. Vera-Olmos, N. Malpica, C. Guttman, S. Vukusic, G. Edan, M. Dojat, M. Styner, S. K. Warfield, F. Cotton, and C. Barillot, "Objective Evaluation of Multiple Sclerosis Lesion Segmentation using a Data Management and Processing Infrastructure," *Nature Scientific Reports*, vol. 8, p. 13650, 2018.
- [11] H. J. Kuijf, J. M. Biesbroek, J. de Bresser, R. Heinen, S. Andermatt, M. Bento, M. Berseth, M. Belyaev, M. J. Cardoso, A. Casamitjana, D. L. Collins, M. Dadar, A. Georgiou, M. Ghafoorian, D. Jin, A. Khademi, J. Knight, H. Li, X. Lladó, M. Luna, Q. Mahmood, R. McKinley, A. Mehrtash, S. Ourselin, B. Park, H. Park, S. H. Park, S. Pezold, E. Puybureau, L. Rittner, C. H. Sudre, S. Valverde, V. Vilaplana, R. Wiest, Y. Xu, Z. Xu, G. Zeng, J. Zhang, G. Zheng, C. Chen, W. van der Flier, F. Barkhof, M. A. Viergever, and G. J. Biessels, "Standardized Assessment of Automatic Segmentation of White Matter Hyperintensities; Results of the WMH Segmentation Challenge," *IEEE Trans. Med. Imag.*, vol. 38, no. 11, pp. 2556–2568, 2019.
- [12] A. M. Mendrik, K. L. Vincken, H. J. Kuijf, M. Breeuwer, W. Bouvy, J. de Bresser, A. Alansary, M. de Bruijn, A. Carass, A. El-Baz, A. Jog, R. Katyali, A. R. Khan, F. van der Lijn, Q. Mahmood, R. Mukherjee, A. van Opbroek, S. Paneri, S. Pereira, M. Persson, M. Rajchl, D. Sarikayan, O. Smedby, C. A. Silva, H. A. Vrooman, S. Vyas, C. Wang, L. Zhaon, G. J. Biessels, and M. A. Viergever, "MRBrainS Challenge: Online Evaluation Framework for Brain Image Segmentation in 3T MRI Scans," *Computational Intelligence and Neuroscience*, vol. 2015, no. Article ID 813696, 2015.
- [13] A. Carass, J. L. Cuzzocreo, S. Han, C. R. Hernandez-Castillo, P. E. Rasser, M. Ganz, V. Beliveau, J. Dolz, I. B. Aved, C. Desrosiers, B. Thyreau, J. E. Romero, P. Coupé, J. V. Manjón, V. S. Fonov, D. L. Collins, S. H. Ying, D. Crocetti, B. A. Landman, S. H. Mostofsky, P. A. Thompson, and J. L. Prince, "Comparing fully automated state-of-the-art cerebellum parcellation from magnetic resonance images," *NeuroImage*, vol. 183, pp. 150–172, 2018.
- [14] T. Rohlfing, "Image similarity and tissue overlaps as surrogates for image registration accuracy: Widely used but unreliable," *IEEE Trans. Med. Imag.*, vol. 31, no. 2, pp. 153–163, 2011.
- [15] J. Chen, Y. Liu, S. Wei, Z. Bian, S. Subramanian, A. Carass, J. L. Prince, and Y. Du, "A survey on deep learning in medical image registration: New technologies, uncertainty, evaluation metrics, and beyond," *Medical Image Analysis*, p. 103385, 2024.
- [16] M. Hoffmann, B. Billot, D. N. Greve, J. E. Iglesias, B. Fischl, and A. V. Dalca, "Synthmorph: learning contrast-invariant registration without acquired images," *IEEE Trans. Med. Imag.*, vol. 41, no. 3, pp. 543–558, 2021.
- [17] R. Jena, D. Sethi, P. Chaudhari, and J. Gee, "Deep learning in medical image registration: Magic or mirage?" in *The Thirty-eighth Annual Conference on Neural Information Processing Systems*, 2024. [Online]. Available: <https://openreview.net/forum?id=IZJ0WYI5YC>
- [18] B. B. Avants, C. L. Epstein, M. Grossman, and J. C. Gee, "Symmetric diffeomorphic image registration with cross-correlation:

- Evaluating automated labeling of elderly and neurodegenerative brain," *Medical Image Analysis*, vol. 12, no. 1, pp. 26–41, 2008.
- [19] G. Balakrishnan, A. Zhao, M. R. Sabuncu, J. Guttag, and A. V. Dalca, "Voxelmorph: a learning framework for deformable medical image registration," *IEEE Trans. Med. Imag.*, vol. 38, no. 8, pp. 1788–1800, 2019.
- [20] A. Torralba and A. A. Efros, "Unbiased look at dataset bias," in *2011 IEEE Conference on Computer Vision and Pattern Recognition (CVPR)*, 2011, pp. 1521–1528.
- [21] K. Zhou, Z. Liu, Y. Qiao, T. Xiang, and C. C. Loy, "Domain generalization: A survey," *IEEE transactions on pattern analysis and machine intelligence*, vol. 45, no. 4, pp. 4396–4415, 2022.
- [22] M. Wang and W. Deng, "Deep visual domain adaptation: A survey," *Neurocomputing*, vol. 312, pp. 135–153, 2018.
- [23] W. D. Penny, K. J. Friston, J. T. Ashburner, S. J. Kiebel, and T. E. Nichols, *Statistical parametric mapping: the analysis of functional brain images*. Elsevier, 2011.
- [24] J. Ashburner and K. J. Friston, "Voxel-based morphometry—the methods," *Neuroimage*, vol. 11, no. 6, pp. 805–821, 2000.
- [25] B. Fischl, "FreeSurfer," *NeuroImage*, vol. 62, no. 2, pp. 774–781, 2012.
- [26] L. Younes, F. Arrate, and M. I. Miller, "Evolutions equations in computational anatomy," *NeuroImage*, vol. 45, no. 1, pp. S40–S50, 2009.
- [27] K. Gregor and Y. LeCun, "Learning fast approximations of sparse coding," in *Proceedings of the 27th international conference on international conference on machine learning*, 2010, pp. 399–406.
- [28] L. Tian, H. Greer, R. Kwitt, F.-X. Vialard, R. S. J. Estépar, S. Bouix, R. Rushmore, and M. Niethammer, "uniGradICON: A foundation model for medical image registration," in *27th International Conference on Medical Image Computing and Computer Assisted Intervention (MICCAI 2024)*, ser. Lecture Notes in Computer Science, vol. 15002, 2024, pp. 749–760.
- [29] Y. Liu, J. Chen, S. Wei, A. Carass, and J. L. Prince, "On Finite Difference Jacobian Computation in Deformable Image Registration," *International Journal of Computer Vision*, pp. 1–11, 2024.
- [30] H. Greer, L. Tian, F.-X. Vialard, R. Kwitt, S. Bouix, R. San Jose Estepar, R. Rushmore, and M. Niethammer, "Inverse consistency by construction for multistep deep registration," in *International Conference on Medical Image Computing and Computer-Assisted Intervention*. Springer, 2023, pp. 688–698.
- [31] L. Tian, H. Greer, F. X. Vialard, R. Kwitt, R. S. J. Estépar, R. Rushmore, N. Makris, S. Bouix, and M. Niethammer, "Gradicon: Approximate diffeomorphisms via gradient inverse consistency," in *2023 IEEE/CVF Conference on Computer Vision and Pattern Recognition (CVPR)*, 2023, pp. 18 084–18 094.
- [32] T. Rohlfing, "Image similarity and tissue overlaps as surrogates for image registration accuracy: Widely used but unreliable," *IEEE Trans. Med. Imag.*, vol. 31, no. 2, pp. 153–163, 2012.
- [33] A. Di Martino, C.-G. Yan, Q. Li, E. Denio, F. X. Castellanos, K. Alaerts, J. S. Anderson, M. Assaf, S. Y. Bookheimer, M. Dapretto *et al.*, "The autism brain imaging data exchange: Towards a large-scale evaluation of the intrinsic brain architecture in autism," *Molecular Psychiatry*, vol. 19, no. 6, pp. 659–667, 2014.
- [34] A. Di Martino, D. O'connor, B. Chen, K. Alaerts, J. S. Anderson, M. Assaf, J. H. Balsters, L. Baxter, A. Beggiano, S. Bernaerts *et al.*, "Enhancing studies of the connectome in autism using the autism brain imaging data exchange II," *Scientific Data*, vol. 4, no. 1, pp. 1–15, 2017.
- [35] "IXI Dataset 2013; Brain Development — brain-development.org," <https://brain-development.org/ixi-dataset>.
- [36] X.-N. Zuo, J. S. Anderson, P. Bellec, R. M. Birn, B. B. Biswal, J. Blautzik, J. Breitner, R. L. Buckner, V. D. Calhoun, F. X. Castellanos *et al.*, "An open science resource for establishing reliability and reproducibility in functional connectomics," *Scientific Data*, vol. 1, no. 140049, pp. 1–13, 2014.
- [37] A. J. Holmes, M. O. Hollinshead, T. M. O'Keefe, V. I. Petrov, G. R. Fariello, L. L. Wald, B. Fischl, B. R. Rosen, R. W. M. J. L. Roffman, J. W. Smoller, and R. L. Buckner, "Brain Genomics Superstruct Project initial data release with structural, functional, and behavioral measures," *Scientific Data*, vol. 2, no. 1, pp. 1–16, 2015.
- [38] S. A. Nastase, Y.-F. Liu, H. Hillman, A. Zadbood, L. Hasenfratz, N. Keshavarzian, J. Chen, C. J. Honey, Y. Yeshurun, M. Regev, M. Nguyen, C. H. C. Chang, C. Baldassano, O. Lositsky, E. Simony, M. A. Chow, Y. C. Leong, P. P. Brooks, E. Micciche, G. Choe, A. Goldstein, T. Vanderwal, Y. O. Halchenko, K. A. Norman, and U. Hasson, "The "narratives" fmri dataset for evaluating models of naturalistic language comprehension," *Scientific Data*, vol. 8, no. 250, 2021.
- [39] A. Babayan, M. Erbey, D. Kumral, J. D. Reinelt, A. M. Reiter, J. Röbbig, H. L. Schaare, M. Uhlig, A. Anwander, P.-L. Bazin *et al.*, "A mind-brain-body dataset of MRI, EEG, cognition, emotion, and peripheral physiology in young and old adults," *Scientific Data*, vol. 6, no. 1, pp. 1–21, 2019.
- [40] A. Sunavsky and J. Poppenk, "Neuroimaging predictors of creativity in healthy adults," *NeuroImage*, vol. 206, p. 116292, 2020.
- [41] P. Li and R. B. Clariana, "Reading comprehension in L1 and L2: An integrative approach," *Journal of Neurolinguistics*, vol. 50, pp. 94–105, 2019.
- [42] D. J. Follmer, S.-Y. Fang, R. B. Clariana, B. J. Meyer, and P. Li, "What predicts adult readers' understanding of STEM texts?" *Reading and Writing*, vol. 31, pp. 185–214, 2018.
- [43] D. P. Orfanos, V. Michel, Y. Schwartz, P. Pinel, A. Moreno, D. Le Bihan, and V. Frouin, "The brainomics/localizer database," *NeuroImage*, vol. 144, pp. 309–314, 2017.
- [44] B. Dufumier, A. Grigis, J. Victor, C. Ambroise, V. Frouin, and E. Duchesnay, "OpenBHB: A large-scale multi-site brain MRI dataset for age prediction and debiasing," *NeuroImage*, vol. 263, p. 119637, 2022.
- [45] D. S. Marcus, T. H. Wang, J. Parker, J. G. Csernansky, J. C. Morris, and R. L. Buckner, "Open Access Series of Imaging Studies (OASIS): Cross-Sectional MRI Data in Young, Middle Aged, Nondemented, and Demented Older Adults," *Jrnl. of Cognitive Neuroscience*, vol. 19, no. 9, pp. 1498–1507, 2007.
- [46] A. Taha, G. Gilmore, M. Abbass, J. Kai, T. Kuehn, J. Demarco, G. Gupta, C. Zajner, D. Cao, R. Chevalier, A. Ahmed, A. Hadi, B. G. Karat, O. W. Stanley, P. J. Park, K. M. Ferko, D. Hemachandra, R. Vassallo, M. Jach, A. Thuraijarah, S. Wong, M. C. tenorio, F. Ogunsanya, A. R. Khan, and J. C. Lau, "Magnetic resonance imaging datasets with anatomical fiducials for quality control and registration," *Scientific Data*, vol. 10, no. 1, p. 449, 2023.
- [47] J. C. Reinhold, B. E. Dewey, A. Carass, and J. L. Prince, "Evaluating the impact of intensity normalization on MR image synthesis," in *Medical Imaging 2019: Image Processing*, vol. 10949. International Society for Optics and Photonics, 2019, p. 109493H.
- [48] Y. Huo, Z. Xu, Y. Xiong, K. Aboud, P. Parvathaneni, S. Bao, C. Bermudez, S. M. Resnick, L. E. Cutting, and B. A. Landman, "3D whole brain segmentation using spatially localized atlas network tiles," *NeuroImage*, vol. 194, pp. 105–119, 2019.
- [49] A. Taha, G. Gilmore, M. Abbass, J. Kai, T. Kuehn, J. Demarco, G. Gupta, C. Zajner, D. Cao, R. Chevalier *et al.*, "Magnetic resonance imaging datasets with anatomical fiducials for quality control and registration," *Scientific Data*, vol. 10, no. 1, p. 449, 2023.
- [50] M. N. Lytle, R. Hammer, and J. R. Booth, "A neuroimaging dataset on working memory and reward processing in children with and without ADHD," *Data in Brief*, vol. 31, p. 105801, 2020.
- [51] M. N. Lytle, D. D. Burman, and J. R. Booth, "A neuroimaging dataset on response inhibition and selective attention in adults and children with and without ADHD," *Data in Brief*, vol. 37, p. 107158, 2021.
- [52] A. C. Nugent, A. G. Thomas, M. Mahoney, A. Gibbons, J. T. Smith, A. J. Charles, J. S. Shaw, J. D. Stout, A. M. Namyst, A. Basavaraj *et al.*, "The NIMH intramural healthy volunteer dataset: A comprehensive MEG, MRI, and behavioral resource," *Scientific Data*, vol. 9, no. 1, p. 518, 2022.
- [53] L. Mahler, J. Steiglechner, B. Bender, T. Lindig, D. Ramadan, J. Bause, F. Birk, R. Heule, E. Charyasz, M. Erb *et al.*, "UltraCortex: Submillimeter ultra-high field 9.4 t brain mr image collection and manual cortical segmentations," *bioRxiv*, pp. 2024–06, 2024.
- [54] V. S. Fonov, A. C. Evans, R. C. McKinstry, C. R. Almli, and D. Collins, "Unbiased nonlinear average age-appropriate brain templates from birth to adulthood," *NeuroImage*, vol. 47, p. S102, 2009.
- [55] M. P. Milham, L. Ai, B. Koo, T. Xu, C. Amiez, F. Balezeau, M. G. Baxter, E. L. Blezer, T. Brochier, A. Chen *et al.*, "An open resource for non-human primate imaging," *Neuron*, vol. 100, no. 1, pp. 61–74, 2018.
- [56] J. Mazziotta, A. Toga, A. Evans, P. Fox, J. Lancaster, K. Zilles, R. Woods, T. Paus, G. Simpson, B. Pike, C. Holmes, L. Collins, P. Thompson, D. MacDonald, M. Iacoboni, T. Schormann, K. Amunts, N. Palomero-Gallagher, S. Geyer, L. Parsons, K. Narr, N. Kabani, G. L. Goulgher, D. Boomsma, T. Cannon, R. Kawashima, and B. Mazoyer, "A probabilistic atlas and ref-

- erence system for the human brain: International Consortium for Brain Mapping (ICBM)," *Phil. Trans. R. Soc. Lond. B*, vol. 356, no. 1412, pp. 1293–1322, 2001.
- [57] B. B. Avants, N. Tustison, and H. Johnson, "Advanced normalization tools (ANTS)," *Insight j*, vol. 2, no. 365, pp. 1–35, 2009.
- [58] T. Zhong, X. Wu, S. Liang, Z. Ning, L. Wang, Y. Niu, S. Yang, Z. Kang, Q. Feng, G. Li *et al.*, "nBEST: Deep-learning-based non-human primates Brain Extraction and Segmentation Toolbox across ages, sites and species," *NeuroImage*, p. 120652, 2024.
- [59] L. R. Dice, "Measures of the Amount of Ecologic Association Between Species," *Ecology*, vol. 26, no. 3, pp. 297–302, 1945.
- [60] A. Carass, S. Roy, A. Gherman, J. C. Reinhold, A. Jesson, T. Arbel, O. Maier, H. Handels, M. Ghafoorian, B. Platel, A. Birenbaum, H. Greenspan, D. L. Pham, C. M. Crainiceanu, P. A. Calabresi, J. L. Prince, W. R. Gray Roncal, R. T. Shinohara, and I. Oguz, "Evaluating White Matter Lesion Segmentations with Refined Sorensen-Dice Analysis," *Nature Scientific Reports*, vol. 10, p. 8242, 2020.
- [61] F. Hausdorff, *Grundzüge der Mengenlehre (Basics of Set Theory)*. Leipzig, Germany: Verlag von Veit & Comp., 1914.
- [62] B. Jian, J. Pan, M. Ghahremani, D. Rueckert, C. Wachinger, and B. Wiestler, "Mamba? catch the hype or rethink what really helps for image registration," in *International Workshop on Biomedical Image Registration*. Springer, 2024, pp. 86–97.
- [63] H. Zhang, X. Chen, R. Hu, D. Liu, G. Li, and R. Wang, "MemWarp: Discontinuity-Preserving Cardiac Registration with Memorized Anatomical Filters," in *27th International Conference on Medical Image Computing and Computer Assisted Intervention (MICCAI 2024)*, ser. Lecture Notes in Computer Science, vol. 15003, 2024, pp. 671–681.
- [64] X. Chen, Y. Xia, N. Ravikumar, and A. F. Frangi, "CAR-Net: unsupervised Co-attention guided registration network for joint registration and structure learning," *arXiv preprint arXiv:2106.06637*, 2021.
- [65] X. Jia, J. Bartlett, T. Zhang, W. Lu, Z. Qiu, and J. Duan, "U-net vs transformer: Is u-net outdated in medical image registration?" in *Machine Learning in Medical Imaging (MLMI 2022) 25th International Conference on Medical Image Computing and Computer Assisted Intervention (MICCAI 2022)*, ser. Lecture Notes in Computer Science, vol. 13583, 2022, pp. 151–160.
- [66] F. Wagner, M. Thies, F. Denzinger, M. Gu, M. Patwari, S. Ploner, N. Maul, L. Pfaff, Y. Huang, and A. Maier, "Trainable joint bilateral filters for enhanced prediction stability in low-dose CT," *Scientific Reports*, vol. 12, no. 1, p. 17540, 2022.
- [67] J. Honkamaa and P. Marttinen, "SITReg: Multi-resolution architecture for symmetric, inverse consistent, and topology preserving image registration," *Machine Learning for Biomedical Imaging (MELBA)*, vol. 2, no. November 2024 Issue, pp. 2148–2194, 2024.
- [68] T. Estienne, M. Vakalopoulou, E. Battistella, T. Henry, M. Leroisseau, A. Leroy, N. Paragios, and E. Deutsch, "MICS: Multi-steps, inverse consistency and symmetric deep learning registration network," *arXiv preprint arXiv:2111.12123*, 2021.
- [69] D. Gu, X. Cao, S. Ma, L. Chen, G. Liu, D. Shen, and Z. Xue, "Pair-wise and group-wise deformation consistency in deep registration network," in *23rd International Conference on Medical Image Computing and Computer Assisted Intervention (MICCAI 2020)*, ser. Lecture Notes in Computer Science, vol. 12263, 2020, pp. 171–180.
- [70] E. J. Hu, Y. Shen, P. Wallis, Z. Allen-Zhu, Y. Li, S. Wang, L. Wang, and W. Chen, "Lora: Low-rank adaptation of large language models," *arXiv preprint arXiv:2106.09685*, 2021.
- [71] Z. Tan, L. Zhang, Y. Lv, Y. Ma, and H. Lu, "GroupMorph: medical image registration via grouping network with contextual fusion," *IEEE Trans. Med. Imag.*, vol. 43, no. 11, pp. 3807–3819, 2024.
- [72] G. Balakrishnan, A. Zhao, M. R. Sabuncu, J. Guttag, and A. V. Dalca, "VoxelMorph: A learning framework for deformable medical image registration," *IEEE Trans. Med. Imag.*, vol. 38, no. 8, pp. 1788–1800, 2019.
- [73] J. Chen, E. C. Frey, Y. He, W. P. Segars, Y. Li, and Y. Du, "Transmorph: Transformer for unsupervised medical image registration," *Medical Image Analysis*, vol. 82, p. 102615, 2022.
- [74] D. Hwang, "FAdam: Adam is a natural gradient optimizer using diagonal empirical Fisher information," *arXiv preprint arXiv:2405.12807*, 2024.
- [75] Y. Hiasa, Y. Otake, M. Takao, T. Matsuoka, K. Takashima, A. Carass, J. L. Prince, N. Sugano, and Y. Sato, "Cross-modality image synthesis from unpaired data using CycleGAN," in *Workshop on Simulation and Synthesis in Medical Imaging (SASHIMI) held in conjunction with the 21st International Conference on Medical Image Computing and Computer Assisted Intervention (MICCAI 2018)*, ser. Lecture Notes in Computer Science, vol. 11037. Springer Berlin Heidelberg, 2018, pp. 31–41.
- [76] H. Greer, L. Tian, F. Vialard, R. Kwitt, S. Bouix, R. San Jose Estepar, R. Rushmore, and M. Niethammer, "Inverse consistency by construction for multistep deep registration," in *26th International Conference on Medical Image Computing and Computer Assisted Intervention (MICCAI 2023)*, ser. Lecture Notes in Computer Science, vol. 14229, 2023, pp. 688–698.
- [77] T. W. Mok and A. S. Chung, "Fast symmetric diffeomorphic image registration with convolutional neural networks," in *2020 IEEE/CVF Conference on Computer Vision and Pattern Recognition (CVPR)*, 2020, pp. 4643–4652.
- [78] H. J. Johnson and G. E. Christensen, "Landmark and intensity-based, consistent thin-plate spline image registration," in *17th Inf. Proc. in Med. Imaging (IPMI 2001)*, ser. Lecture Notes in Computer Science, vol. 2082, 2001, pp. 329–343.
- [79] J.-P. Thirion, "Image matching as a diffusion process: An analogy with Maxwell's demons," *Medical Image Analysis*, vol. 2, no. 3, pp. 243–260, 1998.
- [80] Y. Zhang, Y. Zhao, and Q. Tao, "Improving Instance Optimization in Deformable Image Registration with Gradient Projection," *arXiv preprint arXiv:2410.15767*, 2024.
- [81] T. Yu, S. Kumar, A. Gupta, S. Levine, K. Hausman, and C. Finn, "Gradient surgery for multi-task learning," *Advances in Neural Information Processing Systems*, vol. 33, pp. 5824–5836, 2020.
- [82] H. Wang, Z. Wang, D. Ni, and Y. Wang, "ModeTv2: GPU-accelerated Motion Decomposition Transformer for Pairwise Optimization in Medical Image Registration," *arXiv preprint arXiv:2403.16526*, 2024.
- [83] B. Avants, J. T. Duda, H. Zhang, and J. C. Gee, "Multivariate Normalization with Symmetric Diffeomorphisms for Multivariate Studies," in *10th International Conference on Medical Image Computing and Computer Assisted Intervention (MICCAI 2007)*, ser. Lecture Notes in Computer Science, vol. 4791. Springer Berlin Heidelberg, 2007, pp. 359–366.
- [84] B. Avants and N. Tustison, "ANTs/ANTsR Brain Templates. figshare. Dataset." 2018. [Online]. Available: <https://doi.org/10.6084/m9.figshare.915436.v2>
- [85] A. Klein, J. Andersson, B. A. Ardekani, J. Ashburner, B. Avants, M. C. Chiang, G. E. Christensen, D. L. Collins, J. Gee, P. Hellier, J. H. Song, M. Jenkinson, C. Lepage, D. Rueckert, P. Thompson, T. Vercauteren, R. P. Woods, J. J. Mann, and R. V. Parsey, "Evaluation of 14 nonlinear deformation algorithms applied to human brain MRI registration," *NeuroImage*, vol. 46, no. 3, pp. 786–802, 2009.
- [86] N. J. Tustison, B. B. Avants, L. Flors, T. A. Altes, E. E. de Lange, J. P. Mugler III, and J. C. Gee, "Ventilation-based segmentation of the lungs using hyperpolarized  $^3\text{He}$  MRI," *Jrnl. of Magnetic Resonance Imaging*, vol. 34, no. 4, pp. 831–841, 2011.
- [87] M. P. Heinrich, M. Jenkinson, M. Brady, and J. A. Schnabel, "MRF-based deformable registration and ventilation estimation of lung CT," *IEEE Trans. Med. Imag.*, vol. 32, no. 7, pp. 1239–1248, 2013.
- [88] R. Jena, P. Chaudhari, and J. C. Gee, "FireANTs: Adaptive Riemannian Optimization for Multi-Scale Diffeomorphic Registration," *arXiv preprint arXiv:2404.01249*, 2024.
- [89] Z. Liu, Y. Lin, Y. Cao, H. Hu, Y. Wei, Z. Zhang, S. Lin, and B. Guo, "Swin transformer: Hierarchical vision transformer using shifted windows," in *Proceedings of the IEEE/CVF international conference on computer vision*, 2021, pp. 10 012–10 022.
- [90] J. Chen, E. C. Frey, and Y. Du, "Unsupervised learning of diffeomorphic image registration via transmorph," in *International Workshop on Biomedical Image Registration*. Springer, 2022, pp. 96–102.
- [91] Y. Liu, J. Chen, L. Zuo, A. Carass, and J. L. Prince, "Vector field attention for deformable image registration," *Journal of Medical Imaging*, vol. 11, no. 6, pp. 064 001–064 001, 2024.
- [92] Y. Liu, L. Zuo, S. Han, Y. Xue, J. L. Prince, and A. Carass, "Coordinate Translator for Learning Deformable Medical Image Registration," in *Multiscale Multimodal Medical Imaging (MMMI 2022) held in conjunction with the 25th International Conference on Medical Image Computing and Computer Assisted Intervention (MICCAI 2022)*, ser. Lecture Notes in Computer Science, vol. 13594, 2022, pp. 98–109.